THESIS

THE ROLE OF SURFACE ENERGY AND PLASTICITY IN DETERMINING THE FRACTURE TOUGHNESS OF TANTALUM AND TUNGSTEN

Submitted by

Sajjad Hossain

School of Materials Science & Engineering

In partial fulfillment of the requirements

For the Degree of Master of Science

Colorado State University

Fort Collins, Colorado

Spring 2026

Master's Committee:

Advisor: Christopher R. Weinberger

Justin Sambur
Soham Ghosh

ABSTRACT

THE ROLE OF SURFACE ENERGY AND PLASTICITY IN DETERMINING THE FRACTURE TOUGHNESS OF TANTALUM AND TUNGSTEN

This study quantifies the influence of impurities on the fracture behavior of tungsten (W) and tantalum (Ta) by examining their effects on ideal cleavage energy and fracture toughness. Using density functional theory (DFT), we calculated the reduction in ideal cleavage energy for both the {100} and {110} crystallographic planes of W and Ta due to various impurities, with He, O, P, and S showing significant embrittling effects. These reductions are converted to fracture toughness and incorporated into a dislocation dynamics model to predict changes in the brittle-to-ductile transition (BDT). While both metals exhibit increased brittleness with impurity introduction, tungsten is more sensitive to these effects. Additionally, impurity segregation at grain boundaries, even in ultrapure tungsten, could exacerbate embrittlement due to locally higher impurity concentrations, though experimental evidence for this segregation remains limited. However, small amounts (less than 0.1%) of impurities, as found in ultrapure tungsten, have minimal impact on the fracture behavior of single-crystal tungsten. This work provides a comprehensive assessment of impurity effects on the fracture properties of W and Ta, offering critical insights for high-temperature applications.

ACKNOWLEDGEMENTS

This research work was supported by the U.S. Department of Energy (DOE), Office of Science, Basic Energy Sciences (BES) under the Award DE-SC0022061. This work utilized the Alpine high performance computing resource at the University of Colorado Boulder. Alpine is jointly funded by the University of Colorado Boulder, the University of Colorado Anschutz, Colorado State University, and the National Science Foundation (award No. 2201538).

DEDICATION

I would like to dedicate this thesis to all the people in my life who never stopped believing in me

TABLE OF CONTENTS

LIST OF TABLES

LIST OF FIGURES

Chapter 1

Introduction

Tantalum and tungsten have been widely used in industries such as electronics, cutting tools, aerospace, and medical technology, with the former predominantly used in electronics components such as capacitors and resistors, as well as in cutting tools, and the latter as in high-temperature environments, including light-bulb filaments, welding electrodes, and x-ray tube anodes [1–6]. Despite their adjacent positions on the periodic table and having the same crystal structure – body centered cubic (bcc) – tantalum and tungsten differ significantly with regards to room-temperature ductility and their brittle-to-ductile transition temperature (BDTT); which play crucial roles in their temperature-dependent deformability [7–10]. At room temperature, tungsten displays brittle fracture behavior, whereas tantalum consistently exhibits ductility.

The BDTT for these refractory metals demonstrates distinct ranges depending on whether they are in single or polycrystalline forms. High purity tantalum single crystals exhibit pronounced ductility at temperatures as low as 4.2K [11–13], while in polycrystalline tantalum the BDTT ranges from 23–25K [14,15]. Concurrently, extensive studies on tungsten [16–22] have indicated that polycrystalline samples have BDTT within the range of 350-500K whereas single crystals exhibit a wider range, spanning from 300-650K [23–25].

BDTT experiments primarily measure the fracture toughness of a material at various temperatures to determine the BDT [26,27]. However, the nature of these tests have experimental uncertainty with the calculated stress-intensity factor, the

measured temperature, or even the impurity concentration within the material. As such, it is common to utilize a model that can help interpret the results as well as explain the origins of the BDTT. To model the BDTT, it is common to utilize discrete dislocation dynamics (DDD), which can couple crack-tip fracture behavior along with dislocation nucleation and mobility [28–34]. A 2D discrete dislocation dynamics model is necessary to adequately represent the BDT behavior of the BCC refractory metals like tungsten and tantalum, which exhibits a soft transition that occurs gradually over the range of 100s of Kelvin and is indicative of a transition determined by dislocation mobility limited process, rather than being dislocation nucleation limited [27,35]. The kinetics of the dislocations motion can then be modeled using an enthalpic parameterization of the dislocation velocity [36,37]. This parametrization can be obtained via flow stress experiments performed on the bcc refractory metals as described by Seeger *et al.* [38–41]. These models then simulate the competition between cleavage and plasticity at various temperatures to determine a BDTT, the maximum applied stress intensity factor at fracture, K_{Ic}, and can also be used to separate out the contribution of plasticity on the BDTT. Furthermore, these models can be applied to both intergranular and transgranular fracture, which is observed in the various refractory BCC metals.

To elucidate the disparities in the BDTT, it is important to take a closer look at how metals fracture, whether intergranular or on specific cleavage planes, as the brittle-to-ductile transition temperature is controlled by the competition between cleavage and plasticity. This competition is further exemplified by the predominant fracture mechanisms in tungsten and tantalum, revealing their differing susceptibilities to specific modes of brittle fracture. Both intergranular and transgranular fracture can occur in these metals with the type of fracture being influenced by a

number of factors, including grain shape, size, texture, and impurities [19,21,25,42–47]. Numerous studies have been performed on the fracture type and path in tungsten and tantalum. Both transgranular cleavage and intergranular fracture in tungsten have been observed [24,42,44,46], however in polycrystalline tungsten, brittle fracture is primarily intergranular [42,44,46].

The fracture surfaces of recrystallized tungsten sheets demonstrate that fracture paths vary by recrystallization stage: primary recrystallized specimens predominantly fracture along grain boundaries, while whereas secondary recrystallized specimens mainly exhibit transgranular cleavage, with all brittle cracks initiating at grain boundaries [25]. In rolled, recrystallized, and sintered tungsten samples, the transgranular-to-intergranular fracture ratio is primarily dictated by grain morphology and size distribution, with a pronounced tendency toward intergranular fracture. This predominance is attributed to the lower fracture resistance of grain boundaries relative to the resistance required for transgranular cleavage at room temperature [46]. As it is evident from these studies that tungsten is more susceptible to intergranular fracture, there is some evidence to suggest that tantalum is more prone to transgranular fracture [13,17]. Detailed investigations on tantalum's brittle fracture are limited in the literature, as pure tantalum remains ductile even at liquid helium temperature.

The primary cleavage planes in tantalum identified are {100} and {110} [12,32,33]. Barrett and Bakish [13] observed {110} cleavage facets in Ta samples deformed by impacting at liquid nitrogen temperatures, instances of the {100} planes were also noted. Notably, tantalum exposed to absorbed oxygen, nitrogen, and hydrogen displayed both {100} and {110} cleavage planes. A study at room temperature revealed a sawtooth fracture pattern distinct from typical ductile fractures in pure

tantalum, hinting at a {310} crystallographic cleavage plane [48]. On the other hand, tungsten primarily cleaves on the {100} planes at and below room temperature [8,49–51]. Fracture along {110} has also been observed but not as frequent as {100}, which might be attributed to experimental conditions/setup or the difficulty in initiating {110} cracks [52].

The existance of cleavage on {100} planes, and its preference in some metals like tungsten, has been an active area of research [24, 49,52–55, 57–62]. This is because the {110} plane has slightly lower surface energy compared to that of {100} plane in all the bcc metals as computed by first principle methods [52–55]; so according to Griffith's fracture criterion [56], cleavage on the {110} should be preferred. The preference for {100} fracture has been attributed to an number of factors including plastic work at the crack tip, elastic anisotropy [24], anisotropy associated with lattice trapping [49,57,58], the crack propagation directions for each cleavage plane [33,59], and the availability of slip planes [59–62]. While there is no definitive explanation, both {100} and {110} planes are operative in fracture. Our study exclusively examines the effect of ideal cleavage energy for both {100} and {110} cleavage planes. The impacts of lattice trapping and impurity-induced variations in dislocation mobility are beyond the current scope and will be addressed in future work.

Density functional theory (DFT) has been used to examine the preference for transgranular (V, Nb, Ta, Cr and Fe) and intergranular (W and Mo) fracture. One study interpreted this preference based on ratios of ideal cleavage energies [63] as computed by DFT. Another parameter, R_{CI}, has been used [64,65] to characterize the transition between intergranular and cleavage fracture. This parameter is defined as: $R_{\mathrm{CI}} = \frac{2\gamma_s^{int} - \gamma_b}{2\gamma_s}$ where, γ_s is the surface energy of the crystallographic cleavage plane,

γ_b is the energy of the grain boundary, γ_s^{int} is the surface energy of an intergranular surface. The surface energy of a crystallographic cleavage plane is generally about 20% lower than that of an intergranular surface [64]. R_{CI} was also formulated in terms of the shear modulus μ and bulk modulus K of the material [66–68], as follows: $R_{\mathrm{CI}} = 1.20 - \xi \frac{\mu}{K}$ where ξ is a material-dependent constant, typically close to 1. Using density functional theory (DFT) calculations, R_{CI} has been evaluated for tungsten and tantalum and it suggests a predisposition towards intergranular fracture in tungsten, whereas tantalum leans more towards transgranular fracture [65,66].

Since intergranular fracture is frequently observed, particularly in tungsten, grain boundaries (GBs) are believed to play a critical role in the fracture behavior of both tantalum [11–17] and tungsten [45–54]. Grain boundaries are well known to be regions for impurity segregation [69–71]. These impurities, arising from alloying elements or the environment, tend to accumulate at GBs, potentially impacting the material's fracture mechanisms. Experimental studies have explored these effects, revealing that certain impurities, such as oxygen and carbon, have no significant impact on tungsten's embrittlement [45]. In contrast, the accumulation of phosphorous, particularly in larger grain structures, was highlighted as a notable contributing factor in determining fracture type [44,46], i.e. transgranular or intergranular. Further investigations have indicated that tungsten's fracture behavior remains largely consistent, even with phosphorous concentrations ranging between 20-40 ppm [47]. In another study grain boundary impurities have been observed to exert a minimal influence on the type of fracture and not being potent enough to substantially alter the fracture path [46]. More recently, Tian et al. [72] demonstrated via site-specific microcantilever fracture testing and atom probe tomography that P segregation at GBs in recrystallized tungsten reduces local toughness by approximately threefold,

driving intergranular mode of fracture.

Numerical studies have also been conducted to investigate the effects of impurities on the cohesive behavior of grain boundaries. In tungsten, elements such as carbon and boron enhance the cohesion of $\Sigma5(310)[001]$ GBs [73,74]. Although Setyawan et al. [53,75,76] found that Be, B, C, N, and P improve cohesion in $\Sigma3$ and $\Sigma27$ GBs, other studies [74,77–79] reported that phosphorus generally reduces cohesion and embrittles $\Sigma3$ GBs. However, O, Mg, Si, and S have been found to weaken these boundaries, with O, Si, P, and S particularly detrimental to $\Sigma3(111)$ symmetric tilt GBs [74]. Scheiber *et al.* [63,77,80,81] used the parameter R, which is the ratio of the work of separation along the grain boundary to the surface energy of the preferred cleavage planes $\{001\}$ and evaluated the preference of intergranular fractures in BCC metals (W, Mo, α-Fe). They inferred from ab-initio density functional theory calculations that tungsten's low R value indicates weaker grain boundary cohesion, predisposing it to intergranular failure at low temperatures [63]. They identified alloying elements like B, C, Be, and certain transition metals (e.g., Cr, Mn, Fe) as potential mitigators of this brittleness by enhancing GB cohesion [77,80,81]. In tantalum, similar studies examined the impact of impurities on GB cohesion, focusing on $\Sigma3(111)$ GBs, where the effects of segregation were less severe compared to tungsten [74]. The $\Sigma3(111)$ GBs in tantalum exhibit better resistance to impurity-induced embrittlement compared to tungsten, primarily due to tantalum's lower impurity segregation energies and larger lattice constant, which reduce the adverse effects on GB cohesion [74,82]. Elements like O, Si, P, and S were found to be detrimental to the strength of tantalum GBs, while B, C, N, and Fe were reported to enhance cohesion in these boundaries [74,82,83].

In this study, we examine the role of impurities on affecting the fracture behavior of tantalum and tungsten using combined DFT studies of their ideal cleavage behavior coupled with discrete dislocation dynamics models that can quantify the competition between plasticity and fracture. Specifically, we will quantify the impact of impurities on the fracture toughness of tungsten and tantalum by computing the change in ideal cleavage energy using density functional theory. These energies will be used to calculate the Griffith's fracture toughness, which are implemented as an input into a dislocation dynamics crack model. Discrete dislocation dynamics models will the be used to determine the change in fracture toughness across temperatures as well as the brittle-to-ductile transition temperatures for both tantalum and tungsten as a function of impurity content. Thus, this study will provide new quantitative insights into the interplay between surface energy and ductility, their relative contribution to overall fracture toughness, and the influence of impurities.

Chapter 2

Methodology

In order to compute ideal cleavage energy using DFT, we computed the total energies at 0K using the Vienna ab-initio simulation package (VASP) [84–87], consistent with approaches adopted in previous studies [88–91]. The simulations were done using a plane-wave basis and the projector-augmented wave pseudopotentials [92]. The exchange-correlation energies were computed using the generalized gradient approximation (GGA) using the formulation of Perdew-Burke-Ernzerhof (PBE) [93]. The plane wave cutoff used was set to 600 eV and K-point integration was adjusted to preserve a consistent density of integration points for periodic directions in reciprocal space, maintaining a density of $2\pi * 0.04$ Å^{-1}. The number of valence electrons for the base metals, e.g. tantalum and tungsten, as well as the impurities (e.g. hydrogen, helium, boron, carbon, nitrogen, oxygen, silicon, phosphorus and sulphur) are listed in Table 2.1.

Table 2.1: The elements used in this study and the number of valence electrons used in the DFT simulations.

Element	Electrons	Elements	Electrons
H	$1s^1$	Si	$3s^2 3p^2$
He	$1s^2$	P	$3s^2 3p^3$
B	$2s^2 2p^1$	S	$3s^2 3p$
C	$2s^2 2p^2$	W	$5d^4 6s^2$
N	$2s^2 2p^3$	Ta	$5d^3 6s^2$
O	$2s^2 2p^4$		

To determine the preferential site for interstitial point defects, either octahedral or tetrahedral in the BCC structure, it is typical to compute the defect formation energy (E_{f}). However, the estimation of the chemical potential (μ_{d}) required to calculate the defect formation energy can be difficult in DFT and is often taken as the energy of a pure element in its pure solid state. However, such efforts are not needed to find the preferred interstitial site for further investigation. We only need to investigate the sum of the defect formation energy and chemical potential:

$$\Delta E_{\mathrm{d}} = E_{\mathrm{f}} + \mu_{\mathrm{d}} \qquad \text{for interstitial defects} \tag{2.1a}$$

$$\Delta E_{\mathrm{d}} = E_{\mathrm{f}} + \mu_{\mathrm{d}} - \mu_{\mathrm{h}} \qquad \text{for substitutional defects} \tag{2.1b}$$

which we will call this defect energy for convenience. In order to ensure that the defect energy value is converged, we computed the defect energy as a function of size of the simulation cell. The supercell sizes for defect energy calculations were varied from 1×1×1 to 4×4×4 repeats of the conventional BCC unit cell. Additionally, a 5×4×4 supercell containing 160 host atoms and one impurity (total of 161 atoms) was included, as shown in Figure 2.1(b). The preferred defect sites for each impurity element were identified based on the lowest defect energy configuration.

To simulate {100} ideal cleavage fracture in the two metals, impurity atoms were placed into the preferred interstice and the crystal was cleaved along a {100} plane next to this interstice. The cleavage was modeled by creating a 10 Å gap along the [001] direction in the simulation. The ideal cleavage energy was then computed as: $\gamma_c = \frac{E-E_0}{A}$ where A is the area of the plane, E is the energy of the cleaved crystal and E_0 is the energy of the un-cleaved crystal. However, much like determining the preferred interstice, it is important to ensure the simulation is not affected by the size. We found that three repetitions of the unit cell along the [001] direction were

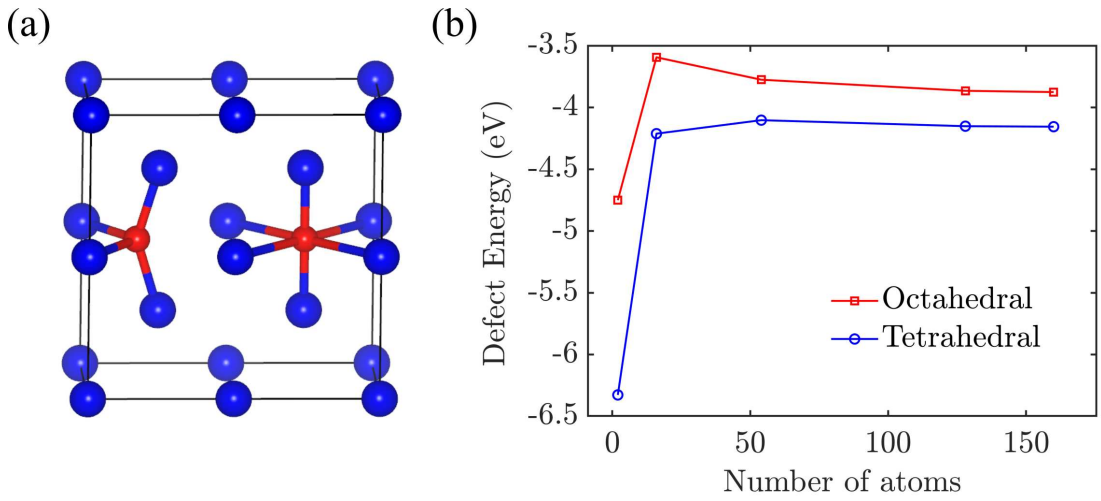

Figure 2.1: (a) The octahedral and tetrahedral interstices in a $1 \times 2 \times 2$ repetition of BCC tungsten unit cell and (b) the defect energies (ΔE_d) of oxygen plotted as a function of the number of atoms in the unit cell.

enough to converge the ideal cleavage energy. This convergence study is shown in Figure 2.2(a), where the ideal cleavage energy converges within 0.01 eV.

In order to vary the density of the impurities on the cleavage plane, we further examined the ideal cleavage energy as we varied the area of the simulation cell on the (001) plane using two distinct supercells with repeat vectors along the [001], [010], and [001] for supercell A as well as [110], [$\bar{1}$10], and [001] directions for supercell B, as illustrated in Figure 2.2(b). The dimensions of the supercells were $Na \times Na \times 3a$ for supercell A and $\sqrt{2}Na \times \sqrt{2}Na \times 3a$ for supercell B where a is lattice constant (for tantalum $a = 3.3087$ Å, for tungsten $a = 3.1726$ Å). The value of N was varied from 2 to 4 in order to achieve desired areal atomic fraction of impurity atoms. By employing $N = 2$, the areal atomic fraction (defined as the ratio of impurity atoms to host metal atoms on cleavage plane, denoted as α) in supercell A is 1/4, while in Supercell B, the areal atomic fraction is 1/8 on the cleavage plane (Figure 2.2(b)).

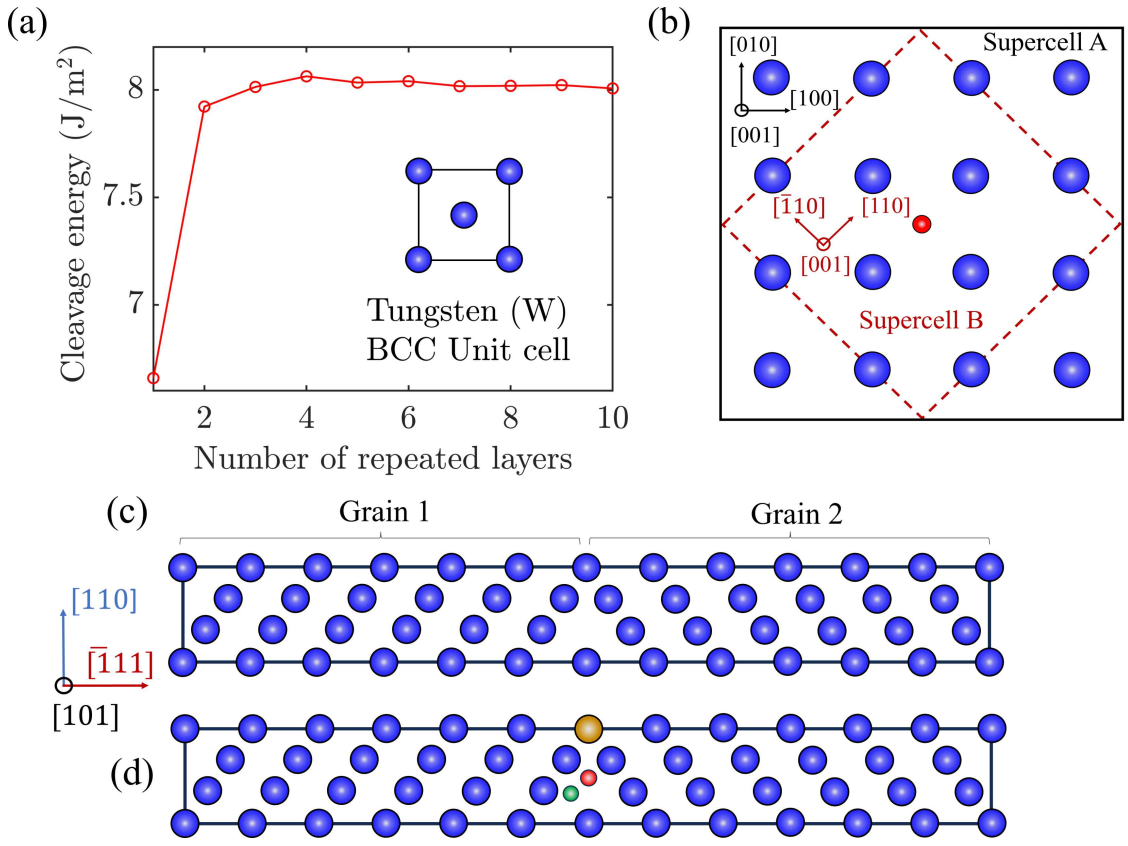

Figure 2.2: (a) The ideal cleavage energy plotted as a function of the layer thickness of tungsten bulk crystal (b) Plane view of the (001) plane with one octahedral interstice filled with an impurity in supercell A ([001],[010], and [001] directions) – corresponding to an areal atomic fraction of 1/16; and supercell B ([110], [$\bar{1}$10], and [001] directions) – corresponding to an areal atomic fraction 1/8. (c) $\sum 3[110](\bar{1}11)$ grain boundary supercell (d) Impurity in a grain boundary in an octahedral (red), tetrahedral (green), and substitutional (orange) site.

The other ratios included in this study were 0, 1/18, 1/8 and 3/8.

In order to quantify how impurities affect the toughness of grain boundaries, we simulated the ideal cleavage of grain boundaries with impurities. We used a GB supercell of a $\sum 3[110](\bar{1}11)$ which has been extensively used in the literature owing to its simple periodic structure and inherent stability and also it is a good

representative model of high energy GBs [63,77,80,81]. The optimal configuration of the $\sum 3[110](\bar{1}11)$ GB used in our study was structurally relaxed using Density functional theory since the cell has only 36 atoms. The simulation cell had repeat vectors pointed along [110], [101] and $[\bar{1}11]$ where the dimension was $\sqrt{2}Na \times \sqrt{2}Na \times 10.39a$ (Figure 2.2(c)). The two adjacent grains share a $\{111\}$ plane, which is the cleavage plane in our simulation. Different impurities were added to the grain boundary in the octahedral, tetrahedral and substitutional sites (Figure 2.2(d)) and, by computing defect energies, their preferential sites were determined. All the impurities preferred to be in interstitial sites and in a particular spot on grain boundaries attributable to the site's larger free volume relative to other positions even for impurities like P, S and Si whose preferential settlement were in substitutional positions. A separation gap of 10 Å along $[\bar{1}11]$ was introduced to compute the ideal cleavage energy with impurities sitting on their preferred sites.

In order to simulate the fracture toughness and brittle-to-ductile transition in Ta and W, we utilized a 2D discrete dislocation dynamics model with a half-space crack tip as described in the work of Tarleton *et al.* [29] as shown in Figure 2.3(a). The main difference from our model and their model is that we neglect the stresses due to bending since we are not specifically simulating a bending test. This model is able to simulate fracture toughness as a function of temperature and the brittle-to-ductile transition temperature by simulating the nucleation of dislocations from Frank-Read sources ahead of the crack tip and subsequently shield the crack tip. In our mode I crack tip plasticity model, edge dislocations provide the shielding traction for crack tip closure, while this process is limited by the mobility of screw dislocations. We use the dislocation mobility from flow stress experiments [39,41] that capture the overall plastic deformation behavior, but are largely controlled by screw dislocation

mobility. By adjusting the position of the dislocation source ahead of the crack tip, we can modulate the contributions of edge and screw dislocations shielding effects and thus correct for the fact that our pure edge dislocation model slightly over-shields the crack tip.

For this work the dislocation sources were placed according to Tarleton *et al.* [29] at $30\overrightarrow{b}$ magnitudes ahead of the crack-tip. The dislocations, once nucleated, move away from the crack-tip according to a dislocation mobility law, $v = v_0 \exp\left(-\frac{H(\tau)}{kT}\right)$, parameterized using the activation enthalpies determined from experiments as shown in Figure 2.3(b). Here, we utilize the antiparabolic enthalpy law [36,37] parameterized by Lim *et al.* [40], $H(\tau) = H_{kp}\left(1 - \frac{\tau}{\tau_p}\right)^2$ for the mobility for Ta and W using the flow stress measurement of Werner [41] and Brunner *et al.* [39], for Ta and W respectively illustrated in Figure 2.+3(b). Here H_{kp} is the enthalpy required to create a kink pair with no applied stress and τ_p is the maximum applied stress required to spotaneously create a kink pair a.k.a Peierl's stress. The velocity pre-fractor, v_0, was chosen to essentially match the BDTT values of Tarleton *et al.* [29] for tungsten. A velocity prefactor for tantalum was chosen based on a relation between the material's Young's modulus and mass density, $v_0 \propto \sqrt{\frac{E}{\rho}}$. Values of the parameters used in the mobility law are listed in Table 2.2.

At each time in the simulation, we compute the stress intensity factor at the crack-tip ($K_{\mathrm{I}}^{\mathrm{tip}}$). If this stress intensity factor for a given applied load exceeds the critical value, Griffith's fracture toughness, then the simulation represents crack propogation and thus brittle fracture as illustrated by the cyan in Figure 2.3(c). Griffith's fracture toughness can be found according to $K_{\mathrm{c}}^{\mathrm{tip}} = \sqrt{\gamma_c E}$, where γ_c is the ideal cleavage energy found according to DFT and E is Young's modulus. This

Table 2.3: The dislocation velocity parameters used in this work. The values for τ_p and H_{kp} were determined via fits to the flow stress experiments performed by Brunner *et al.* [39], Werner [41] and Lim *et al.* [40].

Material	$v_0 \left[\frac{m}{s} \right]$	$\tau_p \; [MPa]$	H_{kp} [eV]
Tungsten	$1 \cdot 10^6$	1038	2.06
Tantalum	$6.5 \cdot 10^5$	320	0.85

value represents the toughness associated with forming the surfaces only. Should the measured stress intensity factor ($K_{\mathrm{I}}^{\mathrm{tip}}$) never reach this Griffith's fracture toughness ($K_{\mathrm{c}}^{\mathrm{tip}}$), Figure 2.3(c) blue cruve, then the crack does not extend and as such the simulation is considered ductile. Thus the brittle-to-ductile transition temperature can be defined as the 1K range between the highest brittle temperature brittle and lowest ductile temperature obtained in these simulations, e.g. the red curve in Figure 2.3(c). Additionally, the maximum applied stress intensity factor at fracture, can be determined for each brittle run which represents the fracture toughness K_{Ic} of the material at that temperature and loading rate. Values of K_{Ic} were found in the 200-400K range for tungsten illustrated in Figure 2.3(d) with the BDTT shown as the horizontal asymptotes.

The aforementioned cleavage simulations provide a method for determining the ideal cleavage energy as a function of the impurity content on the cleavage plane. Thus, this approach leads to a determination of the ideal cleavage energy versus areal atomic fraction. However, in experiments, the impurity content is usually listed as an atomic percent or weight percent. Thus, it is important to convert between these values to make direct comparisons with experiments. This can be done by assuming

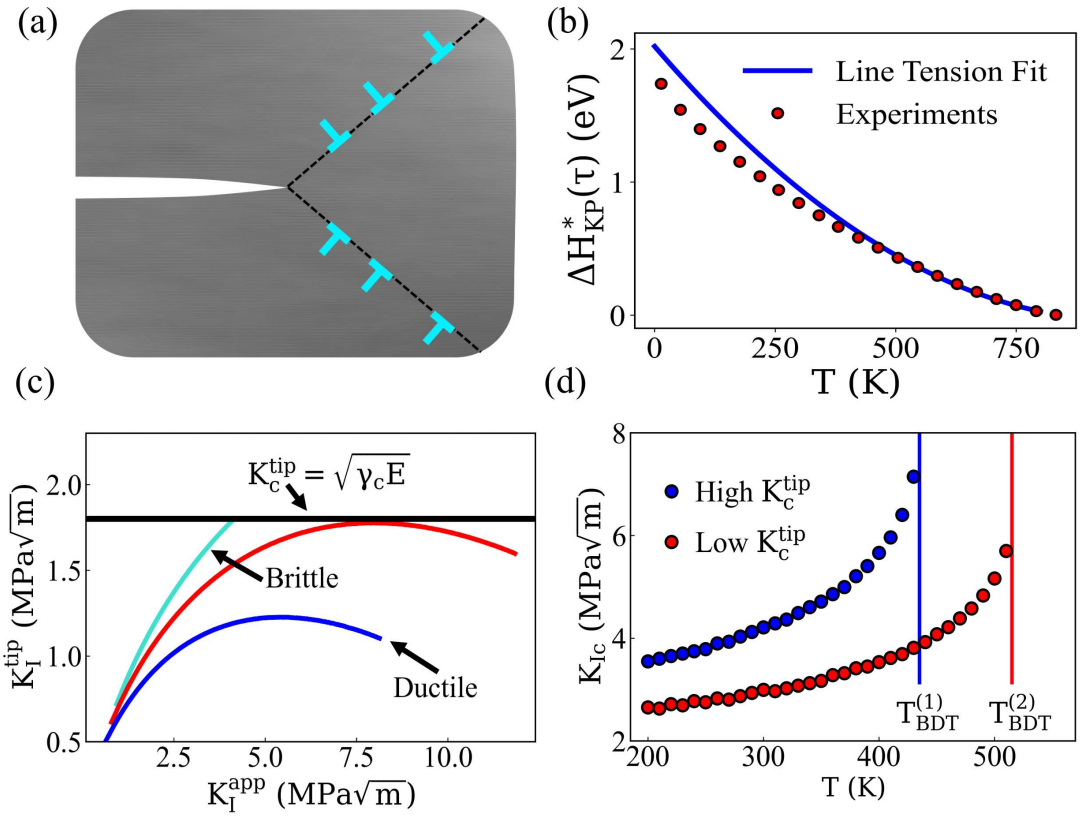

Figure 2.3: (a) Schematic representation of dislocations ahead of the crack tip (b) Enthalpic parameterization of dislocation mobility derived from flow stress experiments, showing the temperature dependence of flow stress compared with experimental data (c) Determination of the applied stress intensity factor at fracture and identification of the corresponding BDTT (d) Fracture toughness K_{Ic} plotted as a function of temperature, with BDTT indicated by vertical lines for two Griffth's fracture toughness K_c^{tip} values.

a uniform distribution of impurity atoms and converting this areal atomic fraction to volume density. For the {100} planes in the BCC crystal (Section 5.1 in Appendix), the atomic fraction of the impurities χ as a measure of impurity concentration, can be related to their areal atomic fraction, α, volume of unit cell V and the atomic volume Ω as:

$$\chi = \frac{\Omega \cdot \alpha^{3/2}}{V} \tag{2.2}$$

Chapter 3

Results and discussions

3.1 Single crystal

3.1.1 Site preference

In our investigation of single-crystal structures of tungsten (W) and tantalum (Ta), we have determined the preferential sites of impurities based on their defect energies. For tungsten single crystals, the defect energies indicate that hydrogen (H) and oxygen (O) preferentially occupy tetrahedral interstitial sites while boron (B), carbon (C), and nitrogen (N) show a preference for octahedral interstitial sites. Helium (He), silicon (Si), phosphorus (P), and sulfur (S) seem to principally reside in substitutional sites. This corroborates earlier findings by Scheiber *et al.* [77] who used defect formation energies to determine preferential sites in tungsten (W) and molybdenum (Mo). In the case of tantalum single crystals, our data suggests that boron (B), carbon (C), nitrogen (N), oxygen (O), and sulfur (S) favor octahedral interstitial sites. Silicon (Si) and phosphorus (P) prefer substitutional sites, while hydrogen (H) and helium (He) appear to favor tetrahedral interstitial sites.

3.1.2 Effect of impurities on ideal cleavage energy

Figure 3.4 shows the effect of the impurities on the ideal cleavage energy of W and Ta on {100} and {110} cleavage planes as a function of the areal atomic fraction, α. The introduction of impurity atoms at any concentration for both W and Ta reduce the single crystal ideal cleavage energy of the metal which should make the material more brittle. Furthermore, we can see that the decrease in ideal cleavage energy γ_c is roughly linear with respect to areal atomic fraction α, at least for small areal atomic

fraction. To make direct comparisons between impurities and between W and Ta, we fit the data to a linear form:

$$\gamma_c = \gamma_c^{'} \cdot \alpha + \gamma_c^0 \tag{3.1}$$

where γ_c^0 is the ideal cleavage energy of the pure metal so that $\gamma_c^{'} \approx \left.\frac{d\gamma_c}{d\alpha}\right|_{\alpha=0}$. To ensure that $\gamma_c^{'}$ is more representative of lower impurity contents that would represent experiments, we weighted the fit towards small value of α. These fits are also shown in Figure 3.5. The evaluation of $\gamma_c^{'}$ allows us to directly compare the effects of impurities on the ideal cleavage energy of the materials. $\gamma_c^{'}$ is plotted in Figure 3.5 versus the impurity type from which we can observe several trends in conjunction with observations in Figure 3.4. First, we note that the ideal cleavage energy of W is more sensitive to impurities than Ta which is noted by the difference in the magnitude of $\gamma_c^{'}$ in Figure 3.5. On average, $\gamma_c^{'}$ is 3.5 times greater in W than Ta on both {100} and {110} cleavage planes which indicates that W will embrittle faster in the presence of impurities than Ta, regardless of the type of impurity. However, this does not immediately resolve the differendes between W and Ta because it is unclear how this change translates to fracture toughness values and BDTT.

No discernible trend was found between the electron configuration of the introduced impurities and the impurity sensitivity, as measured by $\gamma_c^{'}$, for both tungsten and tantalum. However, there are also some important trends to note with regards to the specific types of impurities. Notably, those impurities that have a principal quantum number 2 (namely B, C, N, and O), have very similar sensitivity to impurities. He impurities seem to have a large impact on the ideal cleavage energy in both W and Ta.

The most significant reduction in the ideal cleavage energy, γ_c, is observed at an areal atomic fraction, α of 3/8, corresponding to 11.5 atomic percent. Although the fit

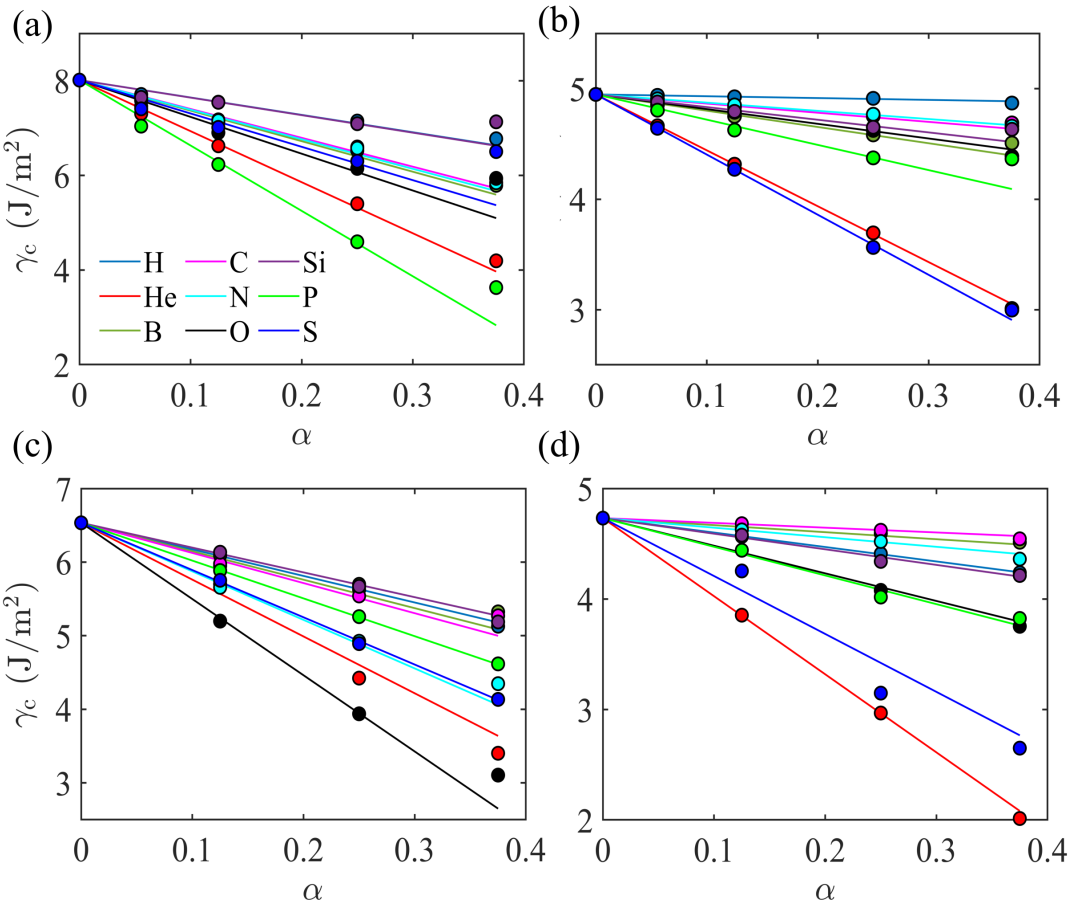

Figure 3.1: The variation of ideal cleavage energies with respect to areal atomic fraction of impurities for {100} planes in (a) tungsten and (b) tantalum and for {110} planes in (c) tungsten and (d) tantalum. The linear relationships are based on equation (4).

in Figure 3.4 emphasizes lower areal atomic fractions, the maximum α used provides a reliable estimate for the upper bounds of brittleness imparted by each impurity. At the maximum areal atomic fraction of 37.5% (3/8 coverage) on {100} cleavage planes, hydrogen results in a 15% decrease in W and a 2% decrease in Ta. The addition of helium markedly influenced both materials, with ideal cleavage energy reductions of 48% for W and 48% for Ta. The addition of elements with a principal quantum number of 2 (B,C,N,O) causes the ideal cleavage energy to decrease by a maximum of 25% in W and 10% in Ta. The introduction of silicon resulted a roughly 10% decrease in the ideal cleavage energy for both W and Ta. Of the impurities

examined, phosphorus exhibited the most pronounced effect on W, leading to a drop of 55% in ideal cleavage energy. In the case of tantalum, sulfur proved most impactful with a decrease of 40%. The impurity sensitivity order for {100} ideal cleavage planes is as follows: for tungsten, P > He > O > S > B > N > C > Si > H, and for tantalum, S > He > P > B > O > Si > C > N > H.

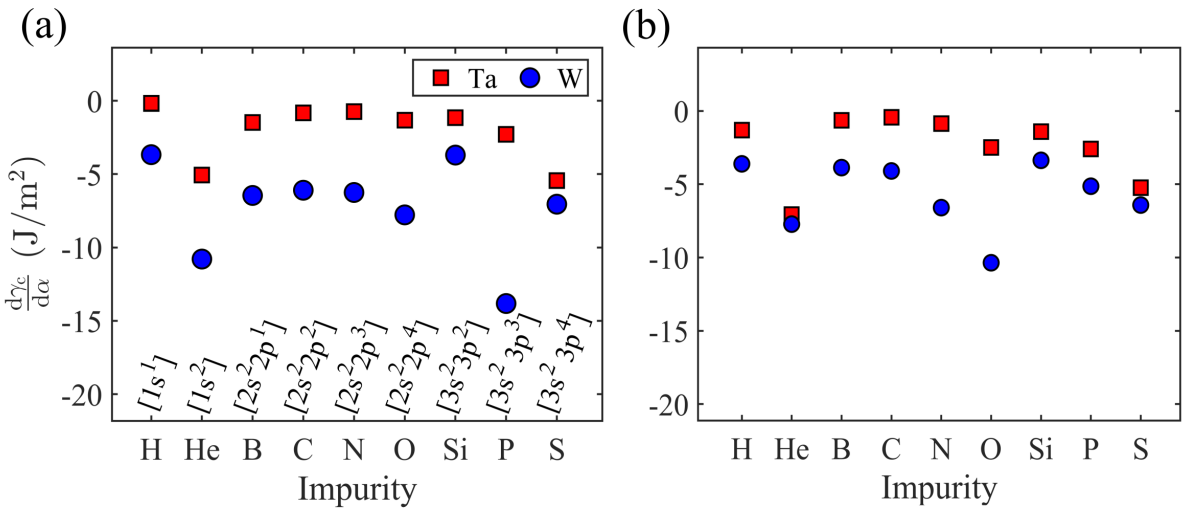

Figure 3.2: The sensitivity of the ideal cleavage energy to impurities on (a) {100} and (b) {110} cleavage planes.

For the {110} cleavage planes, the impurity sensitivity orders are different: for tungsten, O > He > N > S > P > C > B > H > Si; for tantalum, He > S > P > O > Si > H > N > B > C. In general, the ideal cleavage energy of the {110} planes is lower than that of the {100} planes. Without impurities, the ideal cleavage energy is 18.5% and 4.4% lower in W and Ta, respectively. The ideal cleavage energy trends with impurity content on {110} cleavage planes plotted in Figure 3.4(c) and (d), are similar to the observed trends of the {100} planes plotted in Figure 3.4(a) and 3.4(b), which is that impurities reduce γ_c roughly linearly, contributing to increased brittleness. At $\alpha = 3/8$ oxygen is the most detrimental impurity for tungsten on the {110} planes, reducing the ideal cleavage energy by 52.5%, followed by helium at 48%,

while reduction due to other impurities range from 20% to 35%. Notably, hydrogen consistently has the least impact on γ_c for both planes in W. For the {110} planes in tantalum, the strongest embrittlling elements are the same as the {100} with helium and sulfur decreasing γ_c by 57% and 44%, respectively. Elements with a principal quantum number of 2 (B, C, N, O) reduce γ_c by up to 20%. These reductions appear quite modest given the high impurity concentrations. However, it is important to translate this to a change in Griffith's fracture toughness, which we will examined in the next section.

3.1.3 Effect of impurities on Griffith's fracture toughness

In the previous section, the impact of impurities on the ideal cleavage energy of W and Ta was evaluated using DFT, providing quantitative insight into how impurities may influence brittleness. However, fracture toughness is a more widely accepted metric for comparing material resistance to fracture. To this end, we converted the ideal cleavage energy for specific cleavage planes into Griffith's fracture toughness, which represents the intrinsic fracture resistance at 0K, where plasticity is absent as it is thermally activated. While dislocation dynamics simulations can further evaluate the impact of impurities on toughness by accounting for plasticity, these simulations require Griffith's fracture toughness as an input parameter, which is sensitive to impurities.

Figure 3.6 illustrates the relationship between this Griffith's fracture toughness and the atomic percent of impurity atoms embedded within the bulk crystal structures of tungsten and tantalum. It is worth noting that the values used here for pure tungsten, 1.82 MPa$\sqrt{\text{m}}$, are very close to those determined from experiments on single crystals, providing some validation of this approach [33,35,94]. This relationship, *i.e.* the one between $K_{\text{c}}^{\text{tip}}$ and atomic percent χ, is not linear since

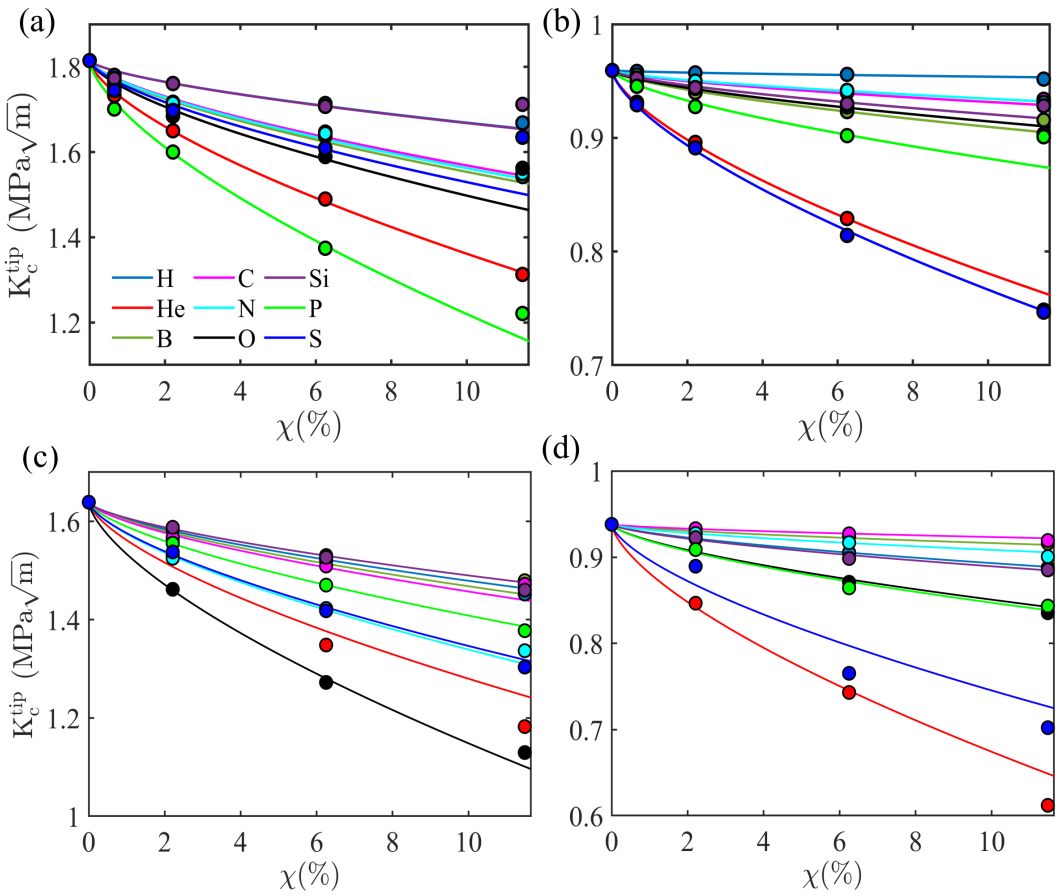

Figure 3.3: The variation of Griffith's fracture toughness with respect to atomic percent for the {100} planes in (a) tungsten and (b) tantalum and for the {110} planes in (c) tungsten and (d) tantalum.

neither the relationship between K_c^{tip} and γ_c nor the relationship between α and χ are linear.

For the {100} cleavage plane in tungsten, Griffith's fracture toughness ranges from 1.82 MPa$\sqrt{m}$ in the absence of impurities to 1.22 MPa$\sqrt{m}$ with 11.5 atomic percent phosphorus (Figure 3.6(a)). On the {110} cleavage plane, the Griffith's fracture toughness varies from 1.64 MPa$\sqrt{m}$ (no impurity) to 1.12 MPa$\sqrt{m}$ in the presence of 11.5 atomic percent oxygen (Figure 3.6(c)). In tantalum, Griffith's toughness on the {100} plane spans from 0.96 MPa$\sqrt{m}$ without impurities to 0.75 MPa$\sqrt{m}$ with

sulfur at 11.5 atomic percent (Figure 3.6(b)). For the {110} plane, the toughness ranges from 0.94 MPa$\sqrt{\text{m}}$ (no impurity) to 0.6 MPa$\sqrt{\text{m}}$ with helium (Figure 3.6(d)), further highlighting the influence of specific impurities on cleavage resistance.

3.2 Grain boundary

3.2.1 Site preference

Within the $\sum 3[110]\,(\bar{1}11)$ grain boundary of tantalum and tungsten, the preferential sites for impurities exhibit less variability compared to their bulk crystal counterparts. Notably, all the impurities consistently gravitated towards a particular interstitial site near the grain boundary. This inclination can be ascribed to the site's large free volume relative to other potential positions.

3.2.2 Impurity influence on ideal cleavage energy and Griffith's fracture toughness

Adding impurities to the cleavage planes of bulk crystal structure generally reduces fracture resistance, and we aimed to determine whether this effect extends to grain boundaries (GBs) as well. As shown in Figure 3.7(a), for tungsten, B, C increase the ideal cleavage energy of the grain boundary. The other impurities (e.g. H, He, N, O, Si, P and S) decreased the ideal cleavage energy. The impact of impurities on Ta is similar, though now N and Si increase the fracture resistance of Ta as well as B and C. The element with the largest impact on fracture resistance is He, which dramatically lowers (by 55%) the fracture resistance of both W and Ta. Figure 3.7(b) shows a bar plot of Griffth's fracture toughness on tungsten and tantalum grain boundaries for the same areal atomic fraction, which follows the same trend as the ideal cleavage energy.

For the grain boundaries, due to computational cost we only addressed a single areal atomic fraction. This is a high areal atomic fraction and thus represents essentially the effect of impurities at a very high concentration. In our DFT simulations, we introduced one impurity atom at the grain boundary and this placement yields an impurity concentration of 5.77 atoms/nm^2 on the grain boundary face. Assuming a random distribution of impurity atoms across both the bulk and grain boundary regions, with no segregation effects, this high areal atomic fraction corresponds to an overall impurity concentration of approximately 2.73 atomic percent. Further details on the assumptions and conversion calculations are provided in the appendix. We will then use only these values to see the impact impurities on the fracture toughness that includes plasticity via our dislocation dynamics models. The resulting estimates will then be conservative estimates on the impact of impurities.

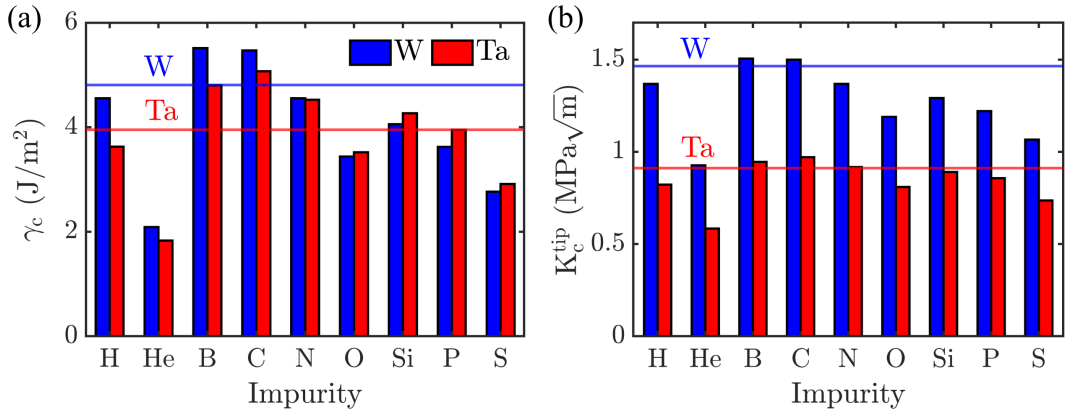

Figure 3.4: The ideal cleavage energy and Griffith's fracture toughness for different impurities on the grain boundaries of tungsten (blue) and tantalum (red). The horizontal lines denotes the values without impurities.

3.3 Impurity influence on fracture toughness and brittle to ductile transition

In order to understand how the reported ideal cleavage energies and their concentration dependence impact the fracture toughness and brittle-to-ductile transitions in these metals, we utilized our discrete dislocation dynamics model to predict both the changes in brittle to ductile transition temperature and fracture toughness changes as a function of the input Griffith's fracture toughness, K_c^{tip}. The plots of the brittle-to-ductile transition temperature (BDTT) as a function of K_c^{tip} are shown below in Figure 3.8(a) for W and Figure 3.8(b) for Ta. This data shows that K_c^{tip} does indeed have an impact on BDTT. Notably, if the ideal cleavage fracture toughness of tungsten drops by a factor of two, the BDTT nearly doubles, indicating a nearly linear indirect relationship between these variables. A similar relationship is seen for tantalum in Figure 3.8(b) where a halving the Griffith's fracture toughness results in nearly a doubling of the BDTT. Similar effects are seen on the fracture toughness itself as shown in Figure 3.8(c) for tungsten with the fracture toughness increasing $2.5 - 3$ times for a doubling of the Griffith's fracture toughness.

While these results indicate that the Griffith's fracture toughness has a strong impact on the BDTT and fracture toughness, these results do not directly indicate how impurity type and impurity content affect these values. To understand this, we have converted the Griffith's fracture toughness to impurity content using the results of Figure 3.8 to produce Figure 3.9 which shows the BDTT plotted as a function of impurity type for impurities in (a) tungsten and (b) tantalum, respectively, and Figure 3.9(c) shows the change in toughness for tungsten. These results show that large impurity concentrations, greater than 1%, can indeed affect the brittle-to-ductile transition temperature and fracture toughness. In fact, from

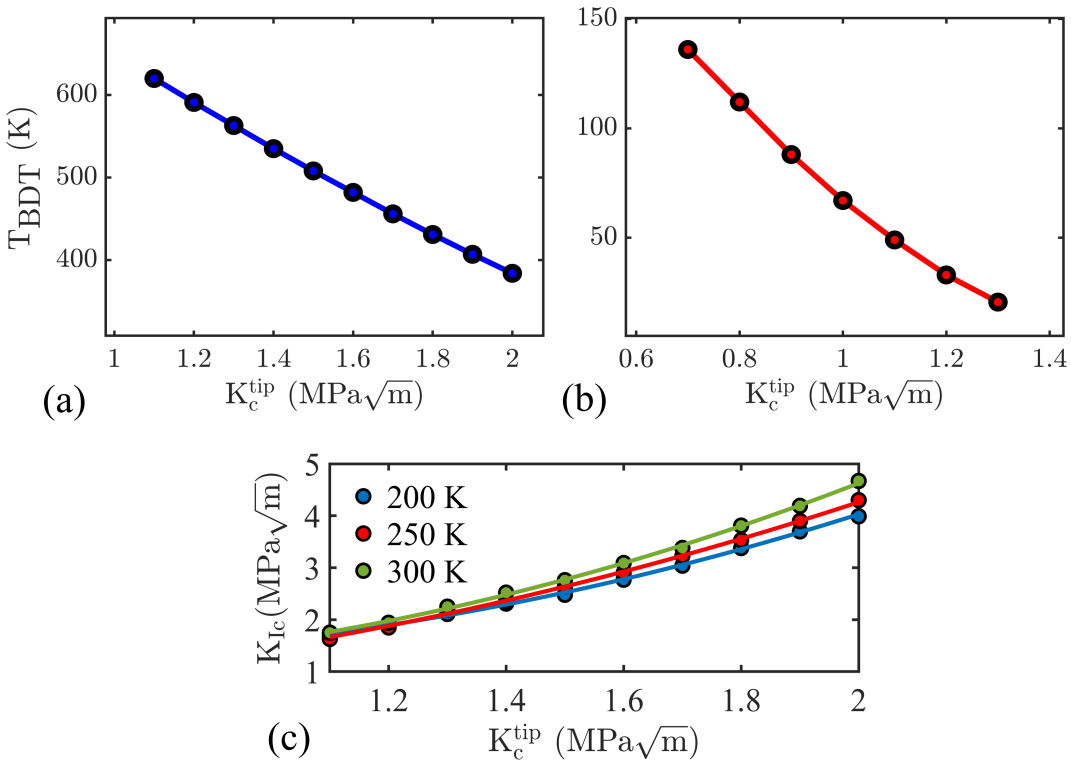

Figure 3.5: (a)-(b) Plot of the brittle-to-ductile transition temperature (T_{BDT}) as a function of Griffith's fracture toughness $K_{\mathrm{c}}^{\mathrm{tip}}$ for tungsten and tantalum. (c) Plot of fracture toughness, K_{Ic}, of tungsten as a function of $K_{\mathrm{c}}^{\mathrm{tip}}$ at temperatures ranging from 200 K to 300 K.

these plots, it is difficult to state that tungsten is more sensitive to impurities than tantalum. However, in either case, it would take enormous impurity concentrations, of order a few percent, to fundamentally alter the brittle-to-ductile transitions of these materials.

While our results demonstrate that impurities can affect the fracture toughness and BDTT of these materials for large impurity concentrations, these are frequently not reported in experiments. In fact, many experiments report impurities in the realm of 10s-100s of ppm and commercially pure tungsten is sold commonly as 99.9% and 99.95%, indicating total impurity content below 0.1%. Thus, it is critical to

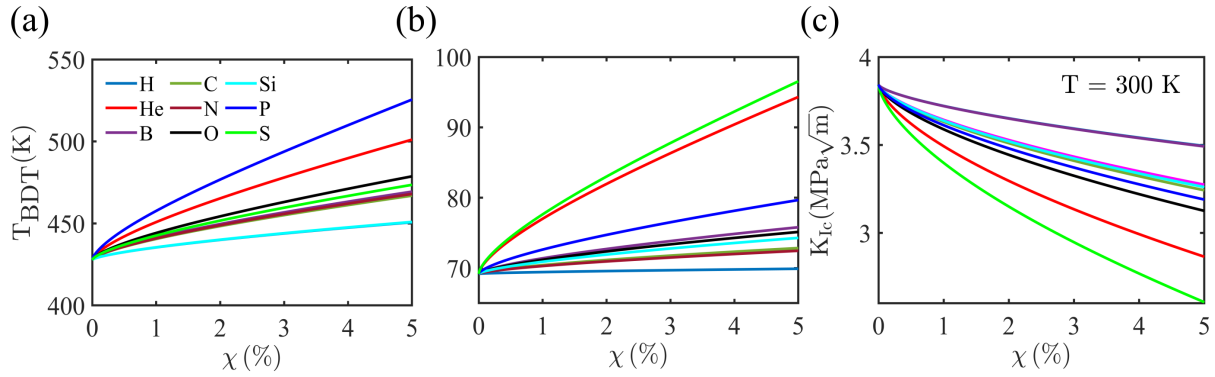

Figure 3.6: The brittle-to-ductile transition temperature (T_{BDT}) plotted as a function of impurity concentration (χ) ranging from 0 to 5% for various elements in (a) tungsten and (b) tantalum. (c) The fracture toughness, K_{Ic}, plotted as a function of impurity concentration (χ) ranging from 0 to 5% for various elements in tungsten at 300K

examine the impact of impurities at small impurity concentrations.

Figure 3.10 shows a plot of the influence of small impurity levels on the (a) BDTT and (b) fracture toughness for three important impurities: hydrogen, oxygen and phosphorous. For 99.9% pure tungsten ($\chi = 0.1\%$), the impact of impurities is very small. The BDTT could change by a few degrees and the fracture toughness could drop a few percent, but nothing that would be reportable in normal experiments as these changes would typically lie in experimental error or measurement uncertainty. For ppm levels of impurities, like oxygen, our results suggest there should be no difference. Hence, these results indicate that impurities are unlikely to alter the fracture behavior of tungsten by altering the nature of its cleavage properties. This is in agreement with experimental results that have found no increases in impurity levels on fracture surfaces of tungsten [46].

Changes in the cleavage of grain boundaries show similar reductions in Griffith's fracture toughness values. If we ignore Helium, which is not a typical impurity in

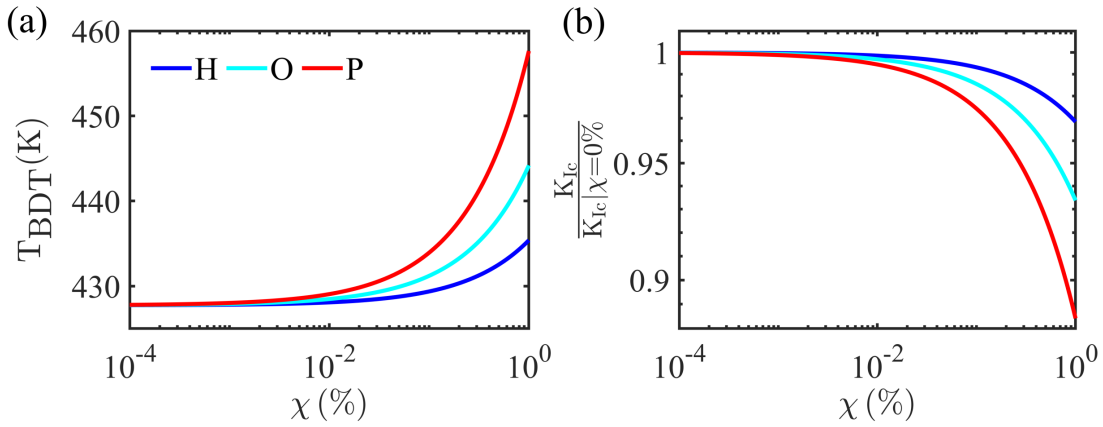

Figure 3.7: (a) The brittle-to-ductile transition temperature (T_{BDT}) plotted as a function of impurity concentration (χ) for hydrogen, oxygen and phosphorus (P) for small values of χ. (b) Fracture toughness ratio $\left(\frac{K_{\mathrm{Ic}}}{K_{\mathrm{Ic}}\ |_{\chi=0\%}}\right)$ as a function of impurity concentration (χ) for the same impurities (H, O, P) on a logarithmic scale.

tungsten, the largest impact on our grain boundary fracture is by sulphur, followed by phosphorous. Sulfur causes a 33% reduction in the Griffith's fracture toughness at our simulated coverage which would result in modest changes in BDTT and fracture toughness according to Figure 3.8(c). Now, if we consider that there is a very different relationship between grain boundary area concentration and bulk concentration, it is possible that higher impurity concentrations would exist at grain boundaries.

The ratio of grain boundary atoms to bulk atoms is about $6\frac{\delta}{D}$ and for a typical coarse grained tungsten crystal with grain diameters (D) of 100 m with an assumed thickness (δ) of 1 nm, the ratio is about 6×10^{-5}. Thus, it is possible impurity atoms at the 10s-100s of ppm levels to segregate to the grain boundary and have high concentrations, say 1% or more. However, if this were true, these concentrations should be relatively easy to detect experimentally. The experimental work to date has not demonstrated clear evidence of high impuritiy concentrations on fracture

surfaces, casting doubt on the role of segregating impurites affect the fracture behavior of tungsten [46]. However, our results clearly demonstrate that high impurity concentrations at the grain boundaries would be necessary to significantly alter the brittle-to-ductile nature of tungsten.

With these results, we can also comment on the potential for grain boundary impurity elements to increase cohesion and improve fracture resistance, as suggested by [53,82]. Our results suggest that boron and carbon can increase the ideal cleavage energy, but the change is very modest. Pan *et al.* [74,82] have shown that boron and carbon increase the ideal cleavage energy and therefore toughen the grain boundary $\sum 3(111)$ and sulphur, phosphus and silicon decrease the GB. This is on par with our results for impurities that embrittle the material, which we have shown is small.

To achieve reasonable toughening, these elements would have to strongly segregate to the grain boundaries in order to appreciably improve toughness. Thus, our results suggest that it is likely not possible to improve the toughness of tungsten appreciably by adding impurities guided by such DFT calculations especially in the absence of knowledge of segregation effects.

Chapter 4

Summary and conclusions

In this paper, we have examined the role impurities play in changing the fracture behavior of tungsten and tantalum by altering the ideal cleavage energy of the material. We utilized density functional theory to compute how the ideal cleavage energy changes as a function of impurity concentration on the {100} and {110} cleavage planes in tungsten and tantalum. These results indicate impurities always decrease the ideal cleavage energy for transgranular cleavage of these two transition metals, making them more brittle. While impurities do change the ideal cleavage energy of tungsten more than tantalum, the differences are not dramatic. The impurities that reduce the ideal cleavage energy the most are helium, oxygen, phosphorous, and sulphur.

Similar to previous studies, we also examined the role of impurities in play in changing the ideal cleavage energy of grain boundaries. We found that impurities can both make tungsten and tantalum more or less brittle, depending on the type of impurity. For tungsten, phosphourous and sulfur decreased the grain boundary ideal cleavage energy the most.

The ideal cleavage energies were converted to the Griffith's fracture toughness, which was used as an input our discrete dislocation dynamics model of the BDT. This model uses the thermally activated nature of plasticity and the Griffith's fracture toughness, which is interpreted as the crack tip toughness $\left(K_{\mathrm{c}}^{\mathrm{tip}}\right)$, to compute the fracture toughness (K_{Ic}) and brittle-to-ductile transition temperature, $\mathrm{T_{BDT}}$. Using this model for tungsten and tantalum, we computed the influence $K_{\mathrm{c}}^{\mathrm{tip}}$ has on the

fracture toughness and BDTT. We found that modest changes in K_c^{tip} has modest changes in BDTT and K_{Ic}. This indicates that large changes in the nature of the brittle-to-ductile transition requires large impurity concentrations. Thus, small amounts of impurities as would exist in ultrapure tungsten, make little impact on the fracture behavior of single crystal tungsten. Furthermore, while tungsten is more sensitive to impurities than tantalum, this difference is not substantial and cannot explain the large differences in the observed brittle-to-ductile transition between these metals.

Our results also indicate that it would be possible to embrittle tungsten grain boundaries through impurities even in ultrapure tungsten. This is because the low concentration of impurities could segregate to the grain boundaries and, due to the large surface area to volume ratio, result in high impurity concentrations at the grain boundaries. However, this would require strong segregation of impurities to the grain boundaries and should be detectible in experiments. Given that experimental evidence suggests that strong segregation does not happen, we can conclude that impurity segregation to grain boundaries and the subsequent reduction of ideal cleavage energy is not the cause of the embrittlement in tungsten.

Despite these conclusions, it is important to note that the effects of impurities cannot be completely ruled out as a significant contributor to the BDT in these materials. The current study has focused only on impurity effects on the ideal cleavage energy. However, the thermally activated nature of plasticity also plays a major role in controlling the BDT. Thus, impurities can also affect dislocation mobility, and hence alter the thermally activated nature of plasticity. This effect on the BDTT also

needs to be evaluated to fully understand the role of impurities and is left for future work.

Author contribution

In this study, I contributed to all primary technical components, including first-principles calculations, methodology development, investigation, formal analysis, data visualization, and preparation of the original manuscript draft. Co-author Hunter K. Brumblay contributed to the methodology section by developing and describing the dislocation dynamics model. Professor Gregory B. Thompson provided funding support and research resources. Professor Christopher R. Weinberger contributed to conceptualization, supervision, investigation guidance, and manuscript review, writing and editing, and also supported the project through funding acquisition and research resources. This work has been published in [103] and is presented here with minor modifications for thesis formatting and clarity.

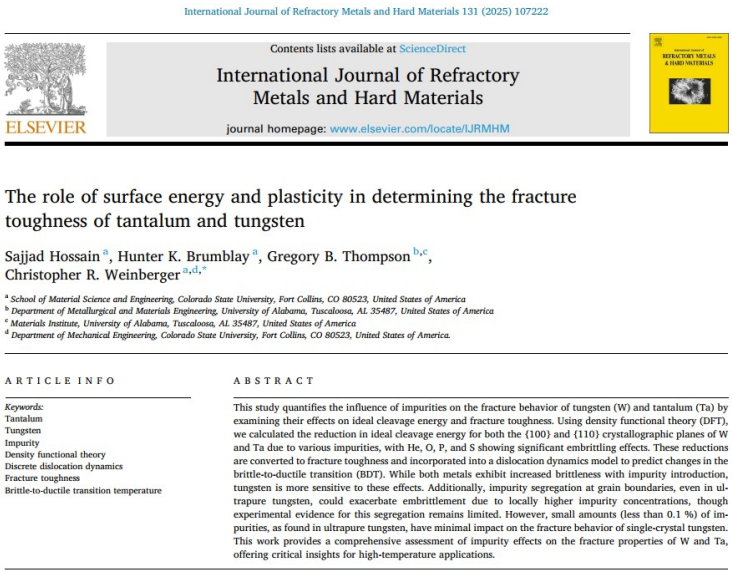

International Journal of Refractory Metals and Hard Materials 131 (2025) 107222

Contents lists available at ScienceDirect

International Journal of Refractory Metals and Hard Materials

journal homepage: www.elsevier.com/locate/IJRMHM

The role of surface energy and plasticity in determining the fracture toughness of tantalum and tungsten

Sajjad Hossain [a], Hunter K. Brumblay [a], Gregory B. Thompson [b,c], Christopher R. Weinberger [a,d,*]

[a] School of Material Science and Engineering, Colorado State University, Fort Collins, CO 80523, United States of America
[b] Department of Metallurgical and Materials Engineering, University of Alabama, Tuscaloosa, AL 35487, United States of America
[c] Materials Institute, University of Alabama, Tuscaloosa, AL 35487, United States of America
[d] Department of Mechanical Engineering, Colorado State University, Fort Collins, CO 80523, United States of America.

ARTICLE INFO

Keywords:
Tantalum
Tungsten
Impurity
Density functional theory
Discrete dislocation dynamics
Fracture toughness
Brittle-to-ductile transition temperature

ABSTRACT

This study quantifies the influence of impurities on the fracture behavior of tungsten (W) and tantalum (Ta) by examining their effects on ideal cleavage energy and fracture toughness. Using density functional theory (DFT), we calculated the reduction in ideal cleavage energy for both the {100} and {110} crystallographic planes of W and Ta due to various impurities, with He, O, P, and S showing significant embrittling effects. These reductions are converted to fracture toughness and incorporated into a dislocation dynamics model to predict changes in the brittle-to-ductile transition (BDT). While both metals exhibit increased brittleness with impurity introduction, tungsten is more sensitive to these effects. Additionally, impurity segregation at grain boundaries, even in ultrapure tungsten, could exacerbate embrittlement due to locally higher impurity concentrations, though experimental evidence for this segregation remains limited. However, small amounts (less than 0.1 %) of impurities, as found in ultrapure tungsten, have minimal impact on the fracture behavior of single-crystal tungsten. This work provides a comprehensive assessment of impurity effects on the fracture properties of W and Ta, offering critical insights for high-temperature applications.

Figure 4.1: Header of the published manuscript [103], including title, full author list and affiliations.

Chapter 5

Appendix

5.1 Areal Atomic Fraction to Atomic Percent Conversion

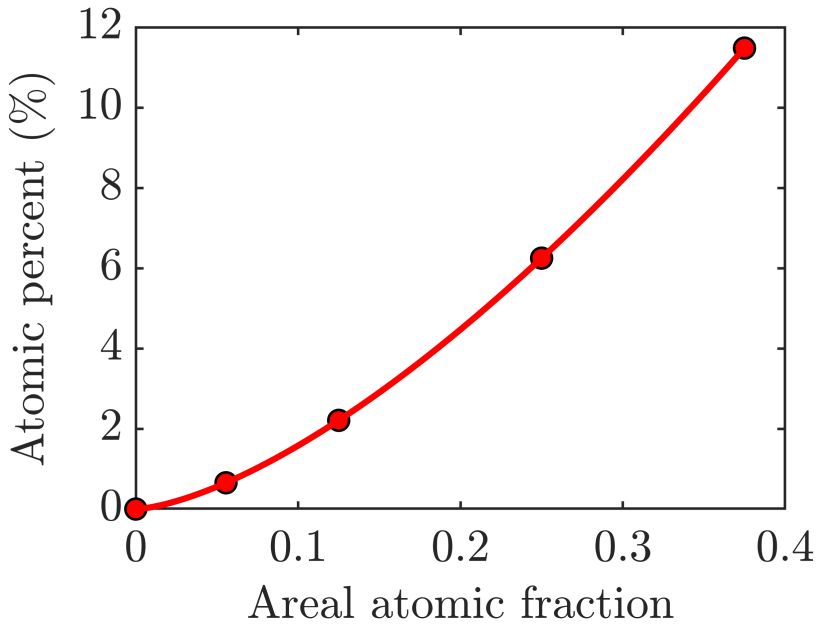

Figure 5.1: Plot of atomic percentage vs areal atomic fraction

Figure 5.1 illustrates the conversion relationship between areal atomic fraction and atomic percent for impurities on the surface of tungsten and tantalum. The x-axis represents the areal atomic fraction, while the y-axis shows the corresponding atomic percent. As shown, the relationship between these two quantities is nonlinear. This curve provides a useful reference for interpreting impurity concentrations in both areal and volumetric terms, facilitating comparison across experimental and computational studies.

5.2 Impurity concentration at the grain boundary

Impurity segregation at grain boundaries generally occurs as a result of thermodynamic preference of impurities to sit at grain boundary sites. Consequently, the degree of equilibrium solute segregation at grain boundaries is determined by both the variety of available site types and the specific segregation energy associated with each site [95]. Experimentally, this could be verified using high-resolution techniques such as atom probe tomography [96] or advanced transmission electron microscopy coupled with energy-dispersive x-ray spectroscopy (EDS) [97,98] or Auger electron spectroscopy [46] can be employed to detect local compositional variations.

In our DFT simulations, we introduced one impurity atom at the grain boundary. We assumed no segregation when calculating atomic concentration instead we assumed a random distribution of impurity atoms between the bulk and grain boundary regions, we can determine the overall impurity concentration (χ_I) in the sample which can be expressed as :

$$\chi_{\mathrm{I}} = \chi_{\mathrm{I}}^{\mathrm{GB}} + \chi_{\mathrm{I}}^{\mathrm{bulk}} \tag{5.1a}$$

$$\chi_{\mathrm{I}} = \frac{\Omega}{V} N_{\mathrm{I}} \tag{5.1b}$$

Where Ω is the atomic volume, V is the volume of the sample, N_I is the number of interstitial impurity atom.

To accurately predict grain boundary concentrations beyond our simple random model, the Langmuir–McLean model [99] could be employed which relates GB impurity concentrations to bulk concentrations via segregation energies. Schieber et al. [100] provide a detailed exposition of how the Langmuir–McLean model can be

applied to quantify grain boundary (GB) segregation in these materials. The McLean isotherm [99] is expressed as

$$\frac{c_{\mathrm{GB}}}{1-c_{\mathrm{GB}}} = \frac{c_{\mathrm{bulk}}}{1-c_{\mathrm{bulk}}} \exp\left(-\frac{\Delta E_{\mathrm{seg}}}{k_{\mathrm{B}}T}\right) \tag{5.2}$$

where c_{GB} is the mole fraction of solute atoms at the GB, c_{bulk} is the mole fraction in the bulk, ΔE_{seg} is the segregation energy (with a negative value indicating a thermodynamic driving force for segregation), k_B is the Boltzmann constant, and T is the absolute temperature. Schieber et al. further elaborate that by measuring or computing ΔE_{seg} from first-principles DFT calculations and knowing the bulk concentration c_{bulk}, the model allows one to predict the equilibrium concentration of solutes at the GB. In our work, while we calculate impurity concentrations with the assumption of a random distribution, invoking the Langmuir–McLean model as discussed by Schieber et al [100] provides a pathway to explicitly predict GB segregation. This model helps relate the DFT-derived segregation energies to observable GB impurity concentrations, offering a thermodynamic framework that bridges our simulation results with experimental measurements.

5.3 Impact of temperature and impurity concentration on fracture toughness

Figure 5.2 shows the impact of impurity concentration on fracture toughness for tungsten at three different temperatures: (a) 200 K, (b) 250 K, and (c) 300 K. As impurity concentration increases, fracture toughness decreases across all temperatures, indicating a consistent embrittling effect. This analysis highlights the temperature-dependent sensitivity of fracture toughness to impurity concentration, critical for understanding tungsten's performance in high-temperature applications.

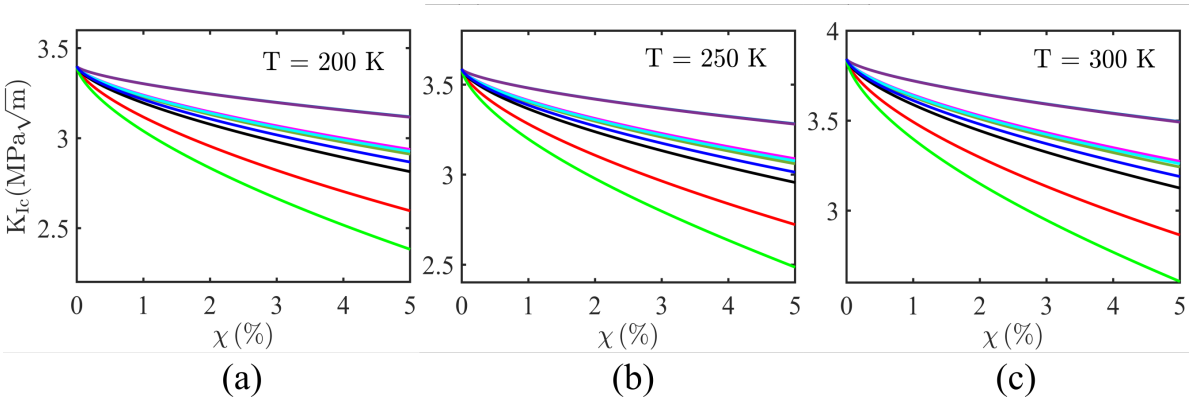

Figure 5.2: Variation of fracture toughness with impurities plotted as a function of concentration for temperatures of (a) 200 K (b) 250 K and (c) 300 K.

5.4 Assumption of anisotropy in Tantalum

We used the polycrystalline averaged Young's modulus for our Ta simulations, including the computation of fracture toughness. We addressed Ta's anisotropy by applying Irwin's method [101] to compute an anisotropy correction factor for the {110} plane relative to the {100} plane under the assumptions of anisotropic elasticity. Although tantalum is inherently anisotropic compared to tungsten, the correction results in less than a 7% variation in the modulus. For example, our calculations yielded the following values:

Table 5.1: Correction factor for W and Ta

Material	$\gamma_c\,[\frac{J}{m^2}]$	$K_c^{\text{tip}}\,[MPa\sqrt{m}]$	Correction factor
W	8.02	1.81	0.99
Ta	4.95	0.91	0.93

This minor adjustment has a negligible impact on Griffith's fracture toughness at the crack tip and an even smaller effect on the dislocation dynamics model [34].

Therefore, our assumption regarding anisotropy in the elastic modulus is reasonable enough.

5.5 Why Boron and Carbon increase GB cohesion?

Boron (B) and Carbon (C) enhance grain boundary cohesion by forming strong, covalent-like bonds with the host metal atoms, which increases the work of separation and improves fracture resistance. According to Cottrell's unified theory [102] for *sp*-interstitial solutes, elements with valence states near the Fermi energy (such as B, C, and N) promote cohesion via covalent bonding. Although the presence of B and C leads to an increase in cleavage energies of the GB interface, the corresponding improvement in Griffith's fracture toughness is approximately 7%, which is relatively modest. Importantly, these impurities may also affect dislocation mobility and, consequently, the plastic behavior of the material—an aspect that we plan to explore in future studies.

5.6 Effect of temperature on cleavage energies

At temperatures approaching the brittle-to-ductile transition (for tungsten which is around 350 – 500K), one would still expect the cleavage energy to remain nearly unchanged compared to its 0 K value. This is because the lattice expansion is minimal in these metals—the low coefficient of thermal expansion (CTE) ensures that the lattice parameters are only slightly altered as temperature increases. As a consequence, the interatomic distances and bonding characteristics that determine the cleavage energy remain almost the same. Even when taking into account additional vibrational (entropic) effects at higher temperatures, these contributions would be modest due to the low CTE, which means that the 0 K DFT predictions for cleavage energy remain a good approximation for conditions near the brittle-to-ductile tran-

sition. Scheiber et al [80] demonstrated the temperature dependence of W-25%atRe cleavage energies also known as work of separation for different temperatures and validates our assumption.

5.7 Impurity Concentration in Pure W

In this study, we consider the impurity elements H, He, B, C, N, O, P, S, and Si in both tantalum and tungsten. These species were selected because they are either commonly present in commercially pure materials due to processing routes (e.g., O, C, N, H, P, S, Si) or are known to play important roles in embrittlement and radiation environments (e.g., He, B). In commercially pure W and Ta (99.9–99.95 %), total impurity levels are typically on the order of a few hundred ppm (<0.05 %), corresponding to 0.01–0.1 at.%. Oxygen is often the dominant interstitial impurity, while phosphorus and sulfur are of particular interest due to their potential grain boundary embrittlement effects. By examining this representative set of impurities, we aim to assess whether realistic impurity species and concentrations can meaningfully alter cleavage energetics and, consequently, fracture behavior in BCC refractory metals.

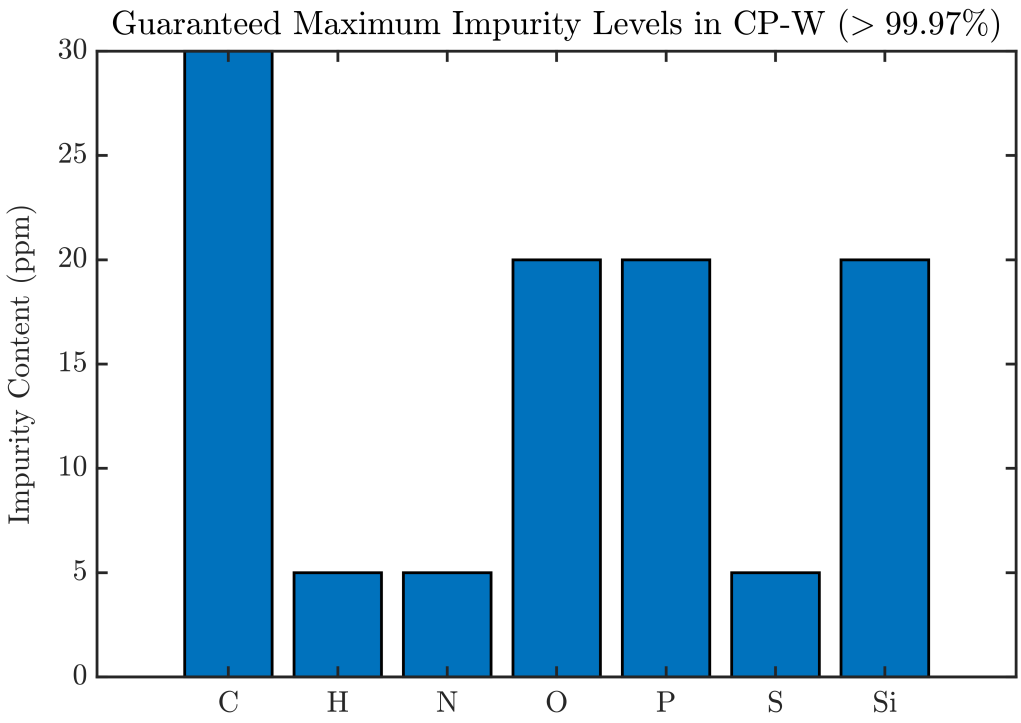

Figure 5.3: Impurity concentration in commercially pure W sample

Chapter 6

Bibliography

[1] R.W. Buckman, New applications for tantalum and tantalum alloys, JOM 52 (2000) 40–41. https://doi.org/10.1007/s11837-000-0100-6.

[2] G.D. Rieck, Tungsten and Its Compounds, Elsevier Science, Burlington, 2013.

[3] H. Qian, Q. Yao, L. Pi, J. Ao, P. Lei, Y. Hu, Current Advances and Applications of Tantalum Element in Infected Bone Defects, ACS Biomater. Sci. Eng. 9 (2023) 1–19. https://doi.org/10.1021/acsbiomaterials.2c00884.

[4] P. Möller, P. Černý, F. Saupé, eds., Lanthanides, tantalum, and niobium: mineralogy, geochemistry, characteristics of primary ore deposits, prospecting, processing, and applications : proceedings of a workshop in Berlin, November 1986, Springer-Verlag, Berlin, 1989.

[5] S.J. Zinkle, N.M. Ghoniem, Operating temperature windows for fusion reactor structural materials, Fusion Eng. Des. 51–52 (2000) 55–71. https://doi.org/10.1016/S0920-3796(00)00320-3.

[6] J. Daintith, The Facts on File Dictionary of Chemistry, Facts on File, 2005.

[7] Fracture toughness properties of aerospace materials, in: Introd. Aerosp. Mater., Elsevier, 2012: pp. 454–468. https://doi.org/10.1533/9780857095152.454.

[8] A. Pineau, Fracture: Cleavage, in: Encycl. Mater. Sci. Technol., Elsevier, 2001: pp. 3279–3283. https://doi.org/10.1016/B0-08-043152-6/00584-2.

[9] D. Şopu, A. Foroughi, M. Stoica, J. Eckert, Brittle-to-Ductile Transition in Metallic Glass Nanowires, Nano Lett. 16 (2016) 4467–4471.

[10] W. Kang, M.T.A. Saif, In Situ Study of Size and Temperature Dependent Brittle-to-Ductile Transition in Single Crystal Silicon, Adv. Funct. Mater. 23 (2013) 713–719. https://doi.org/10.1002/adfm.201201992.

[11] J.A. Shields, S.H. Goods, R. Gibala, T.E. Mitchell, Deformation of high purity tantalum single crystals at 4.2 K, Mater. Sci. Eng. 20 (1975) 71–81. https://doi.org/10.1016/0025-5416(75)90132-9.

[12] S. Takeuchi, K. Maeda, Slip in high purity tantalum between 0.7 and 40 K, Acta Metall. 25 (1977) 1485–1490. https://doi.org/10.1016/0001-6160(77)90078-5.

[13] C.S. Barrett, B. R., Twinning and cleavage in tantalum, Trans. Am. Inst. Min. Metall. Pet. Eng. 212 (1958) 122–123.

[14] J.R. Davis, Tantalum and Tantalum Alloys, in: Corros. Weldments, ASM International, 2006, n.d.: p. 164.

[15] J.R. Davis, Tantalum and Tantalum Alloys, in: Alloy. Underst. Basic, ASM International, 2001, n.d.: p. 324.

[16] J.W. Pugh, Refractory metals: Tungsten, tantalum, columbium, and rhenium, JOM 10 (1958) 335–339. https://doi.org/10.1007/BF03398215.

[17] J.H. Bechtold, Tensile properties of annealed tantalum at low temperatures, Acta Metall. 3 (1955) 249–254. https://doi.org/10.1016/0001-6160(55)90060-2.

[18] G.L. Davis, Embrittlement of Tungsten Wires by Contaminants, Nature 181 (1958) 1198–1198. https://doi.org/10.1038/1811198a0.

[19] P.J. Burdon, G.L. Davis, Embrittlement of tungsten and of molybdenum, Nat. Publ. Group (n.d.). https://www.nature.com/articles/185455a0.

[20] C.S. Barrett, Metallurgy at low temperatures, Trans. Am. Soc. Met. 49 (1957) 53–117.

[21] A.W. Funkenbusch, F. Bacon, D. Lee, The influence of microstructure on fracture of drawn tungsten wire, Metall. Trans. A 10 (1979) 1085–1091. https://doi.org/10.1007/BF02811654.

[22] P.L. Raffo, Yielding and fracture in tungsten and tungsten-rhenium alloys, J. Common Met. 17 (1969) 133–149. https://doi.org/10.1016/0022-5088(69)90047-2.

[23] M. Grujicic, H. Zhao, G.L. Krasko, Atomistic simulation of 3 (111) grain boundary fracture in tungsten containing various impurities, Int. J. Refract. Met. Hard Mater. 15 (1997) 341–355. https://doi.org/10.1016/S0263-4368(97)87508-7.

[24] D. Hull, P. Beardmore, A.P. Valintine, Crack propagation in single crystals of tungsten, Philos. Mag. J. Theor. Exp. Appl. Phys. 12 (1965) 1021–1041. https://doi.org/10.1080/14786436508228132.

[25] P. Gumbsch, J. Riedle, A. Hartmaier, H.F. Fischmeister, Controlling Factors for the Brittle-to-Ductile Transition in Tungsten Single Crystals, Science 282 (1998) 1293–1295. https://doi.org/10.1126/science.282.5392.1293.

[26] M. Brede, P. Haasen, The brittle-to-ductile transition in doped silicon as a model substance, Acta Metall. 36 (1988) 2003–2018. https://doi.org/10.1016/0001-6160(88)90302-1.

[27] P.D. Warren, The brittle-ductile transition in silicon: The influence of pre-existing dislocation arrangements, Scr. Metall. 23 (1989) 637–642. https://doi.org/10.1016/0036-9748(89)90504-8.

[28] P.B. Hirsch, S. Roberts, J. SAMUELS, The dynamics of dislocation generation at crack tips and the ductile-brittle transition, Scr. Metall. 21 (1987) 1523–1528. https://doi.org/10.1016/0036-9748(87)90294-8.

[29] E. Tarleton, S.G. Roberts, Dislocation dynamic modelling of the brittle–ductile transition in tungsten, Philos. Mag. 89 (2009) 2759–2769.

[30] A. Giannattasio, Z. Yao, E. Tarleton, S.G. Roberts, Brittle–ductile transitions in polycrystalline tungsten, Philos. Mag. 90 (2010).

[31] A. Giannattasio, S.G. Roberts, Strain-rate dependence of the brittle-to-ductile transition temperature in tungsten, Philos. Mag. 87 (2007) 2589–2598. https://doi.org/10.1080/14786430701253197.

[32] J. Reiser, A. Hartmaier, Elucidating the dual role of grain boundaries as dislocation sources and obstacles and its impact on toughness and brittle-to-ductile transition, Sci. Rep. 10 (2020) 2739. https://doi.org/10.1038/s41598-020-59405-5.

[33] P. Gumbsch, Brittle fracture and the brittle-to-ductile transition of tungsten, J. Nucl. Mater. 323 (2003) 304–312. https://doi.org/10.1016/j.jnucmat.2003.08.009.

[34] H.K. Brumblay, G.B. Thompson, C.R. Weinberger, Insights into the soft brittle-to-ductile transition from discrete dislocation dynamics, Comput. Mater. Sci. 247 (2025) 113503. https://doi.org/10.1016/j.commatsci.2024.113503.

[35] S.G. Roberts, Modelling the brittle to ductile transition in single crystals, NATO ASI Ser. E Appl. Sci.-Adv. Study Inst. 308 (1996) 409–434.

[36] A.S. Argon, 4 THE LATTICE RESISTANCE, in: A. Argon (Ed.), Strength. Mech. Cryst. Plast., Oxford University Press, 2007: p. 0. https://doi.org/10.1093/acprof:oso/9780198516002.003.0004.

[37] D. Caillard, J.L. Martin, eds., Chapter 7 - The Peierls–Nabarro Mechanism in Covalent Crystals, in: Pergamon Mater. Ser., Pergamon, 2003: pp. 227–277. https://doi.org/10.1016/S1470-1804(03)80037-8.

[38] F. Ackermann, H. Mughrabi, A. Seeger, Temperature-and strain-rate dependence of the flow stress of ultrapure niobium single crystals in cyclic deformation, Acta Metall. 31 (1983) 1353–1366.

[39] D. Brunner, Comparison of flow-stress measurements on high-purity tungsten single crystals with the kink-pair theory, Mater. Trans. JIM 41 (2000) 152–160.

[40] H. Lim, C.C. Battaile, J.D. Carroll, B.L. Boyce, C.R. Weinberger, A physically based model of temperature and strain rate dependent yield in BCC metals: Implementation into crystal plasticity, J. Mech. Phys. Solids 74 (2015) 80–96.

[41] M. Werner, Temperature and strain-rate dependence of the flow stress of ultrapure tantalum single crystals, Phys. Status Solidi A 104 (1987) 63–78. https://doi.org/10.1002/pssa.2211040105.

[42] K. Farrell, A.C. Schaffhauser, J.O. Stiegler, Recrystallization, grain growth and the ductile-brittle transition in tungsten sheet, J. Common Met. 13 (1967) 141–155. https://doi.org/10.1016/0022-5088(67)90177-4.

[43] A. Gilbert, A fractographic study of tungsten and dilute tungsten-rhenium alloys, J. Common Met. 10 (1966) 328–343. https://doi.org/10.1016/0022-5088(66)90133-0

[44] Tran-Huu-Loi, J.P. Morniroli, M. Gantois, M. Lahaye, Brittle fracture of polycrystalline tungsten, J. Mater. Sci. 20 (1985) 199–206. https://doi.org/10.1007/BF00555913

[45] A. Joshi, D.F. Stein, Intergranular brittleness studies in Tungsten Using Auger Spectroscopy, Metall. Trans. 1 (1970) 2543–2546. https://doi.org/10.1007/BF03038381

[46] B. Gludovatz, S. Wurster, T. Weingärtner, A. Hoffmann, R. Pippan, Influence of impurities on the fracture behaviour of tungsten, Philos. Mag. 91 (2011) 3006–3020. https://doi.org/10.1080/14786435.2011.558861.

[47] H. Danninger, F. Knoll, B. Lux, Phosphorus embrittlement of tungsten heavy alloys, Int J Refract Hard Met 4 (1985) 92–96.

[48] B.L. Boyce, B.G. Clark, P. Lu, J.D. Carroll, C.R. Weinberger, The Morphology of Tensile Failure in Tantalum, Metall. Mater. Trans. A 44 (2013) 4567–4580. https://doi.org/10.1007/s11661-013-1814-8.

[49] J. Riedle, P. Gumbsch, H.F. Fischmeister, Cleavage Anisotropy in Tungsten Single Crystals, Phys. Rev. Lett. 76 (1996) 3594–3597.

[50] M.J.S. Spencer, A. Hung, I.K. Snook, I. Yarovsky, Density functional theory study of the relaxation and energy of iron surfaces, Surf. Sci. 513 (2002) 389–398. https://doi.org/10.1016/S0039-6028(02)01809-5.

[51] M. Methfessel, D. Hennig, M. Scheffler, Trends of the surface relaxations, surface energies, and work functions of the $4d$ transition metals, Phys. Rev. B 46 (1992) 4816–4829. https://doi.org/10.1103/PhysRevB.46.4816.

[52] W.R. Tyson, R.A. Ayres, D.F. Stein, Anisotropy of cleavage in B.C.C. transition metals, Acta Metall. 21 (1973) 621–627. https://doi.org/10.1016/0001-6160(73)90071-0.

[53] W. Setyawan, R.J. Kurtz, Effects of transition metals on the grain boundary cohesion in tungsten, Scr. Mater. 66 (2012) 558–561.

[54] E. Aghemenloh, J.O. Umukoro, S.O. Azi, S. Yusuf, J.O.A. Idiodi, Surface energy calculation of bcc metals using the analytical equivalent crystal theory method, Comput. Mater. Sci. 50 (2011) 3290–3296. https://doi.org/10.1016/j.commatsci.2011.06.014

[55] J.Y. Lee, M.P.J. Punkkinen, S. Schönecker, Z. Nabi, K. Kádas, V. Zólyomi, Y.M. Koo, Q.-M. Hu, R. Ahuja, B. Johansson, J. Kollár, L. Vitos, S.K. Kwon, The surface energy and stress of metals, Surf. Sci. 674 (2018) 51–68. https://doi.org/10.1016/j.susc.2018.03.008.

[56] A.A. Griffith, The phenomena of rupture and flow in solids, Philos. Trans. R. Soc. Lond. Ser. Contain. Pap. Math. Phys. Character 221 (1921) 163–198. https://doi.org/10.1098/rsta.1921.0006.

[57] P. Hiremath, S. Melin, E. Bitzek, P.A.T. Olsson, Effects of interatomic potential on fracture behaviour in single- and bicrystalline tungsten, Comput. Mater. Sci. 207 (2022) 111283. https://doi.org/10.1016/j.commatsci.2022.111283.

[58] J.J. Möller, E. Bitzek, Fracture toughness and bond trapping of grain boundary cracks, Acta Mater. 73 (2014) 1–11. https://doi.org/10.1016/j.actamat.2014.03.035

[59] S. Kohlhoff, P. Gumbsch, H.F. Fischmeister, Crack propagation in b.c.c. crystals studied with a combined finite-element and atomistic model, Philos. Mag. A 64 (1991) 851–878. https://doi.org/10.1080/01418619108213953.

[60] R. Chang, An atomistic study of fracture, Int. J. Fract. Mech. 6 (1970) 111–125. https://doi.org/10.1007/BF00189819.

[61] J. Mei, Y. Ni, J. Li, The effect of crack orientation on fracture behavior of tantalum by multiscale simulation, Int. J. Solids Struct. 48 (2011) 3054–3062. https://doi.org/10.1016/j.ijsolstr.2011.06.022.

[62] T. Suzudo, K. Ebihara, T. Tsuru, Brittle-fracture simulations of curved cleavage cracks in α -iron: A molecular dynamics study, AIP Adv. 10 (2020) 115209. https://doi.org/10.1063/5.0026659.

[63] D. Scheiber, R. Pippan, P. Puschnig, L. Romaner, *Ab initio* calculations of grain boundaries in bcc metals, Model. Simul. Mater. Sci. Eng. 24 (2016) 035013. https://doi.org/10.1088/0965-0393/24/3/035013.

[64] D. François, A. Pineau, A. Zaoui, Mechanical Behaviour of Materials: Volume II: Fracture Mechanics and Damage, Springer Science & Business Media, 2012.

[65] A. Pineau, A.A. Benzerga, T. Pardoen, Failure of metals I: Brittle and ductile fracture, Acta Mater. 107 (2016) 424–483. https://doi.org/10.1016/j.actamat.2015.12.034

[66] A.H. Cottrell, Strengths of grain boundaries in pure metals, Mater. Sci. Technol. 5 (1989) 1165–1167. https://doi.org/10.1179/mst.1989.5.12.1165.

[67] A.H. Cottrell, Strength of grain boundaries in impure metals, Mater. Sci. Technol. 6 (1990) 325–329. https://doi.org/10.1179/mst.1990.6.4.325.

[68] A.H. Cottrell, Strengthening of grain boundaries by segregated interstitials in iron, Mater. Sci. Technol. 6 (1990) 121–123. https://doi.org/10.1179/mst.1990.6.2.121

[69] G. Dehm, J. Cairney, Implication of grain-boundary structure and chemistry on plasticity and failure, MRS Bull. 47 (2022) 800–807. https://doi.org/10.1557/s43577-022-00378-3

[70] T. Watanabe, Grain boundary engineering: historical perspective and future prospects, J. Mater. Sci. 46 (2011) 4095–4115. https://doi.org/10.1007/s10853-011-5393-z.

[71] D. Raabe, M. Herbig, S. Sandlöbes, Y. Li, D. Tytko, M. Kuzmina, D. Ponge, P.-P. Choi, Grain boundary segregation engineering in metallic alloys: A pathway to the design of interfaces, Curr. Opin. Solid State Mater. Sci. 18 (2014) 253–261. https://doi.org/10.1016/j.cossms.2014.06.002.

[72] C. Tian, Y. Ma, A. Ghafarollahi, P. Patil, G. Dehm, E. Bitzek, M. Rasinski, J.P. Best, Segregation-enhanced grain boundary embrittlement of recrystallised tungsten evidenced by site-specific microcantilever fracture, Acta Mater. 259 (2023) 119256. https://doi.org/10.1016/j.actamat.2023.119256.

[73] H. Zhou, S. Jin, Y. Zhang, G. Lu, First-principles study of carbon effects in a tungsten grain boundary: site preference, segregation and strengthening, Sci. China Phys. Mech. Astron. 54 (2011) 2164–2169. https://doi.org/10.1007/s11433-011-4495-6.

[74] Z. Pan, L.J. Kecskes, Q. Wei, The nature behind the preferentially embrittling effect of impurities on the ductility of tungsten, Comput. Mater. Sci. 93 (2014) 104–111. https://doi.org/10.1016/j.commatsci.2014.06.036.

[75] W. Setyawan, R.J. Kurtz, *Ab initio* study of H, He, Li and Be impurity effect in tungsten Σ3{1 1 2} and Σ27{5 5 2} grain boundaries, J. Phys. Condens. Matter 26 (2014) 135004. https://doi.org/10.1088/0953-8984/26/13/135004.

[76] W. Setyawan, R.J. Kurtz, Effects OF B, C, N, O, P and S impurities on tungsten Σ27 [110]{552} and Σ3 [110]{112} grain boundaries, Pacific Northwest National Lab.(PNNL), Richland, WA (United States), 2013.

[77] D. Scheiber, R. Pippan, P. Puschnig, L. Romaner, *Ab initio* search for cohesion-enhancing impurity elements at grain boundaries in molybdenum and tungsten, Model. Simul. Mater. Sci. Eng. 24 (2016) 085009. https://doi.org/10.1088/0965-0393/24/8/085009.

[78] P.A.T. Olsson, P. Hiremath, S. Melin, Atomistic investigation of the impact of phosphorus impurities on the tungsten grain boundary decohesion, Comput. Mater. Sci. 219 (2023) 112017. https://doi.org/10.1016/j.commatsci.2023.112017.

[79] P. Hiremath, S. Melin, P.A.T. Olsson, Phosphorus driven embrittlement and atomistic crack behavior in tungsten grain boundaries, Comput. Mater. Sci. 244 (2024) 113194. https://doi.org/10.1016/j.commatsci.2024.113194.

[80] D. Scheiber, V.I. Razumovskiy, P. Puschnig, R. Pippan, L. Romaner, Ab initio description of segregation and cohesion of grain boundaries in W–25 at.% Re alloys, Acta Mater. 88 (2015) 180–189. https://doi.org/10.1016/j.actamat.2014.12.053.

[81] D. Scheiber, R. Pippan, P. Puschnig, A. Ruban, L. Romaner, Ab-initio search for cohesion-enhancing solute elements at grain boundaries in molybdenum and tungsten, Int. J. Refract. Met. Hard Mater. 60 (2016) 75–81. https://doi.org/10.1016/j.ijrmhm.2016.07.003.

[82] Z. Pan, Comparative study of the effect of impurities on the ductility of tantalum and tungsten based on atomistic and first principles calculations, 2012. https://ui.adsabs.harvard.edu/abs/2012PhDT.....42P (accessed August 26, 2024).

[83] G.L. Krasko, Effect of metalloid impurities on grain boundary stability in tantalum. Final report, October 1994-September 1995, Army Research Lab., Aberdeen Proving Ground, MD (United States), 1996.

[84] G. Kresse, J. Hafner, *Ab initio* molecular dynamics for liquid metals, Phys. Rev. B 47 (1993) 558–561. https://doi.org/10.1103/PhysRevB.47.558.

[85] G. Kresse, J. Hafner, Norm-conserving and ultrasoft pseudopotentials for first-row and transition elements, J. Phys. Condens. Matter 6 (1994) 8245–8257. https://doi.org/10.1088/0953-8984/6/40/015.

[86] G. Kresse, J. Furthmüller, Efficiency of ab-initio total energy calculations for metals and semiconductors using a plane-wave basis set, Comput. Mater. Sci. 6 (1996) 15–50. https://doi.org/10.1016/0927-0256(96)00008-0.

[87] G. Kresse, J. Furthmüller, Efficient iterative schemes for *ab initio* total-energy calculations using a plane-wave basis set, Phys. Rev. B 54 (1996) 11169–11186. https://doi.org/10.1103/PhysRevB.54.11169.

[88] P. Lazar, R. Podloucky, Cleavage fracture of a crystal: Density functional theory calculations based on a model which includes structural relaxations, Phys. Rev. B 78 (2008) 104114. https://doi.org/10.1103/PhysRevB.78.104114.

[89] M. Geng, H. Jónsson, Density Functional Theory Calculations and Thermodynamic Analysis of the Forsterite Mg_2 SiO_4 (010) Surface, J. Phys. Chem. C 123 (2019) 464–472. https://doi.org/10.1021/acs.jpcc.8b09047.

[90] H. Yu, G.B. Thompson, C.R. Weinberger, The role of chemistry and bonding in regulating fracture in multiphase transition metal carbides and nitrides, Extreme Mech. Lett. 17 (2017) 1–6. https://doi.org/10.1016/j.eml.2017.09.004.

[91] S. Hossain, G.B. Thompson, C.R. Weinberger, Exploring fracture anisotropy in tantalum carbide compounds: A density functional theory approach, J. Am. Ceram. Soc. 107 (2024) 7758–7769. https://doi.org/10.1111/jace.19917.

[92] P.E. Blöchl, Projector augmented-wave method, Phys. Rev. B 50 (1994) 17953–17979. https://doi.org/10.1103/PhysRevB.50.17953.

[93] J.P. Perdew, K. Burke, M. Ernzerhof, Generalized Gradient Approximation Made Simple, Phys. Rev. Lett. 77 (1996) 3865–3868.

[94] J. Ast, M. Göken, K. Durst, Size-dependent fracture toughness of tungsten, Acta Mater. 138 (2017) 198–211. https://doi.org/10.1016/j.actamat.2017.07.030.

[95] M. Wagih, C.A. Schuh, Learning Grain-Boundary Segregation: From First Principles to Polycrystals, Phys. Rev. Lett. 129 (2022) 046102. https://doi.org/10.1103/PhysRevLett.129.046102.

[96] A. Gupta, X. Zhou, G.B. Thompson, G.J. Tucker, Role of grain boundary character and its evolution on interfacial solute segregation behavior in nanocrystalline Ni-P, Acta Mater. 190 (2020) 113–123. https://doi.org/10.1016/j.actamat.2020.03.012.

[97] X. Zhou, R. Darvishi Kamachali, B.L. Boyce, B.G. Clark, D. Raabe, G.B. Thompson, Spinodal Decomposition in Nanocrystalline Alloys, Acta Mater. 215 (2021) 117054. https://doi.org/10.1016/j.actamat.2021.117054.

[98] X. Zhou, X. Yu, T. Kaub, R.L. Martens, G.B. Thompson, Grain Boundary Specific Segregation in Nanocrystalline Fe(Cr), Sci. Rep. 6 (2016) 34642. https://doi.org/10.1038/srep34642.

[99] D. McLean, A. Maradudin, *Grain Boundaries in Metals*, Phys. Today 11 (1958) 35–36. https://doi.org/10.1063/1.3062658.

[100] D. Scheiber, M.N. Popov, L. Romaner, Temperature dependence of solute segregation energies at W GBs from first principles, Scr. Mater. 222 (2023) 115059. https://doi.org/10.1016/j.scriptamat.2022.115059.

[101] G.C. Sih, P.C. Paris, G.R. Irwin, On cracks in rectilinearly anisotropic bodies, Int. J. Fract. Mech. 1 (1965) 189–203. https://doi.org/10.1007/BF0018685.

[102] A.H. Cottrell, Unified theory of effects of segregated interstitials on grain boundary cohesion, Mater. Sci. Technol. 6 (1990) 806–810. https://doi.org/10.1179/mst.1990.6.9.806

[103] S. Hossain, H. K. Brumblay, G. B. Thompson, C. R. Weinberger, The role of surface energy and plasticity in determining the fracture toughness of tantalum and tungsten, International Journal of Refractory Metals and Hard Materials, Volume 131, 2025, 107222, ISSN 0263-4368, https://doi.org/10.1016/j.ijrmhm.2025.107222